Characterization of Carrier Dynamics in Metal Oxide Nanostructures and Tellurophenes

by

Benjamin Daniel Wiltshire

A thesis submitted in partial fulfillment of the requirements for the degree of

Master of Science

in

Microsystems and Nanodevices

Department of Electrical and Computer Engineering
University of Alberta

Abstract

Research was undertaken into the charge carrier dynamics of TiO_2 nanotube and nanowire structures, which have potential in many technological applications and are already used in solar cells, OLED's, photocatalysts, and biomedical applications. Using a combination of Time of Flight, Photoconductivity, IV, CV, and Time Resolved Microwave Conductivity, the charge carrier dynamics of TiO_2 nanostructures were measured and later improved upon using a self-assembled monolayer surface for passivation, with mobility improving by a factor of almost 1000. The Time of Flight and Time Resolved Microwave Conductivity are explained in detail and can be used quickly, easily, and with a wide variety of materials to measure important material properties that are difficult to find using other methods.

Organic Tellurophenes were also investigated using quantitative photoluminescence (PL) measurements such as quantum yield measurements and time resolved photoluminescence. The Tellurophenes were previously uncharacterized and only available in small quantitites. They were found to have unique properties such as triplet-decay leading to phosphorescent light emission which was tunable and with a relatively high quantum yield. The Tellurophenes were also found to have relatively high carrier mobilities after doping as high as $1.1 \times 10^{-4} cm^2 V^{-1} s^{-1}$.

Preface

Some of the research conducted for this thesis forms part of a research collaboration, led by Professor Dr. Karthik Shankar and Dr. Eric Rivard at the University of Alberta. The tellurophene material mentioned in section 1.2.3, 3.3, and 3.4 was made by Gang He. The results from section 3.3 were published as He, Gang, BD Wiltshire et al. "Phosphorescence within tellurophenes and color tunable tellurophenes under ambient conditions." *Chemical Communications* 51.25 (2015): 5444-5447. A different tellurophene material from the same group was treated with iodine and used in section 3.4 and published as Mohammadpour, Arash, BD Wiltshire, et al. "Charge transport, doping and luminescence in solution-processed, phosphorescent, air-stable tellurophene thin films." *Organic Electronics* 39 (2016): 153-162.

Results in section 3.2 is part of a collaboration between the Shankar group and the Daneshmand group in the Electrical and Computer Engineering Department at the University of Alberta. The microwave resonators were designed, fabricated, tested, and simulated by Mohammad Zarifi and the Daneshmand group. The results shown in section 3.2 were published as Zarifi, M. H., et al. "Time-resolved microwave photoconductivity (TRMC) using planar microwave resonators: Application to the study of long-lived charge pairs in photoexcited titania nanotube arrays." *The Journal of Physical Chemistry C* 119.25 (2015): 14358-14365.

Results in section 3.1 was published as Mohammadpour, Arash, et al. "Majority carrier transport in single crystal rutile nanowire arrays." *physica status solidi (RRL)-Rapid Research Letters* 8.6 (2014): 512-516. and Mohammadpour, A., BD Wiltshire, et al. "100-fold improvement in carrier drift mobilities in alkanephosphonate-passivated monocrystalline TiO2 nanowire arrays." *Nanotechnology* 28.14 (2017): 144001.

Acknowledgements

I would first like to thank Dr. Shankar, my supervisor, who was constantly a guiding and helping presence in every task and challenge I faced in my work. He was an excellent source of knowledge and advice and constantly pushed me to better myself and improve. He has taught me so much since I was a student in his EE 250 class and I am forever grateful for his patience, kindness, and direction over all these years.

I would also like to thank my mentors and friends in the university who helped guide my work and taught me the ins and outs of research: Dr. Mojgan Daneshmand, Dr. Eric Rivard, Dr. Vladimir Michaelis, Arash Mohammadpour, Samira Farsinezhad, Abdelrahman Askar, Mourad Benlamri, Piyush Kar, Yun Zhang, Kaveh Ahadi, Ujwal Thakur, Mohammad Zarifi, Gang He, Lhing Hsuan-Hseieh, Prashant Waghmare, Joel Boulet, Himani Sharma, Najia Mahdi, Ryan Kisslinger, Weidi Hua, and so many more.

Thanks as well to my family and friends, who support and encourage me always in whatever I do. Their love and patience gives me the spirit to improve myself and keep moving forward and I am forever grateful.

Table of Contents

List of Tables

Table Description Page Number

List of Figures

Figure Description **Page Number**

List of Abbreviations

Abbreviation	Description	First use
UV	Ultraviolet……..…..……..2	
PL	Photoluminescence Measurement……..…….…….…2	
SILAR	Successive Ionic Layer Adsorption and Reaction……...…….6	
FTO	Fluorine-doped Tin Oxide…….7	
SCLC	Space Charge Limited Current…….9	
SAM	Self Assembled Monolayer……...9	
EG	Ethylene Glycol……..…..16	
UV-Vis	Ultraviolet-Visible Spectroscopy……..……..……22	
XRD	X-ray Diffraction……..22	
TEM	Transmission Electron Microscopy……...22	
ODPA	Octadecyl Phosphonic Acid……..24	
FTIR	Fourier Transform Infrared Spectroscopy……....25	
DRIFTS	Diffuse Reflection Infrared Fourier Transform……25	
SEM	Scanning Electron Microscopy……..24	
TOF	Time of Flight……26	
PC	Photoconductivity Measurement……...…30	
BPin	Pinacolboronate……...……...……34	
CW	Continuous Wave……..…..…35	
TRMC	Time Resolved Microwave Conductivity……..39	
VNA	Vector Network Analyzer……...41	
TNTAM	Titanium Nanotube Array Membrane……..……...58	

Chapter One: Introduction

1.1 Overview

It has been almost 60 years since December 29th 1959, when Richard Feynman gave his keynote speech "There's Plenty of Room at the Bottom"[1], introducing the ideas and promises of nanotechnology, and how a new nanosized world was waiting to be explored just beyond the limits of the current technology. This was a time when rockets and space flight dominated the science headlines, and the integrated circuit had been invented the same year but was only in its infancy. Over time though, Feynman's forecast turned out to be correct as nanotechnology has made a huge impact on human achievement over the last half decade.

In the past, stone was the most useful material for tools and weapons because it was abundant and could be made into rough shapes. Then bronze was discovered, and we found that with heat we could make a metal alloy stronger than what we had before, and more useful. Later, the Iron Age and then the invention of steel kept pushing humanity towards more and more capabilities, until we had almost the entire periodic table at our disposal. A defining feature of nanotechnology is that the properties of a material can change on very small size scales, leading to new ideas and applications. Many of these applications are truly unique in that only by building at such small dimensions do they become possible, making this truly an opportunity for cutting edge research to do more with (much) less.

Described as the science of materials between 1 and 100 *nm* in dimension, nanotechnology has become a huge field in science and engineering. The commercial applications of nanotechnology are large and growing, with roles in food packaging[2-4], non-stick and waterproof coatings[5-7], household appliances and clothing[8-10], sensors[11-13], medical applications[14-16], photocatalysis and CO_2 photoreduction[17-19], LED's and OLED's[20-22], solar cells[23-25], and of course the transistor: the building block of all modern digital devices. But interest in nanotechnology is not just based on what has been done, but rather what can be done; and research in the field will likely continue for at least another 60 years.

1.2 Introduction to Titanium Dioxide Nanostructures

Titanium dioxide is a compound with the chemical formula TiO_2, it is formed naturally in nature in three phases: anatase, rutile, and brookite[26], though only the first two phases are commonly used and researched. TiO_2 is a large bandgap semiconductor; anatase with a bandgap of 3.0 *eV* and rutile with a band gap of 3.2 *eV*[27]. Each phase has unique properties and a unique method of growth, allowing for more flexibility when making nanostructures. Both phases of TiO_2 are chemically stable, low-cost, safe for humans, and both can be formed from amorphous phase TiO_2 with heating. The crystal structures of anatase and rutile are shown below in Figure 1.

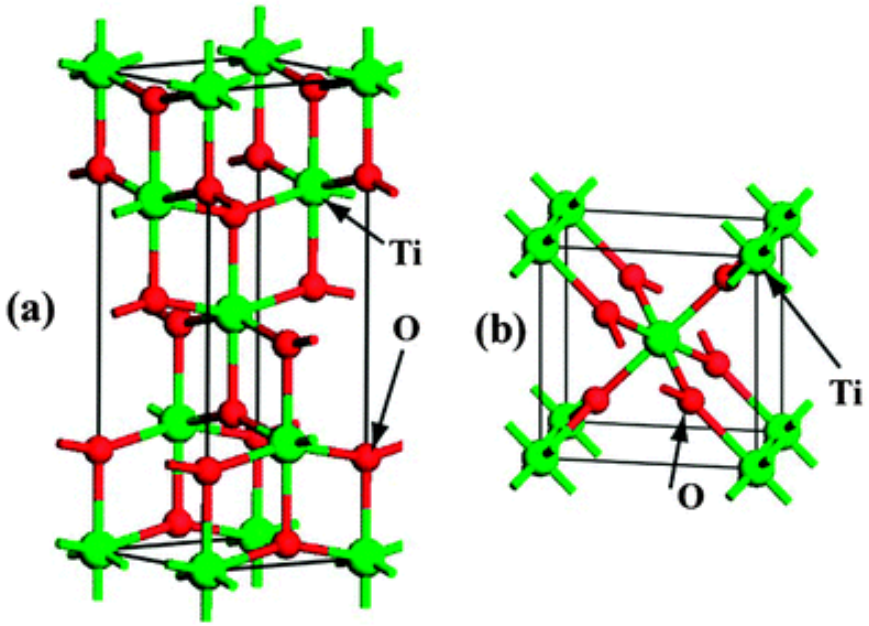

Figure 1: Anatase (a) and Rutile (b) crystal structures of TiO_2. Adapted from [28]

Titanium dioxide has been commonly used in many modern applications including photocatalysis[6, 29], Ultraviolet (UV) sensing[30], solar cells[31, 32], LEDs/OLEDs[33], self-cleaning surfaces[34, 35], water treatment[36, 37], and CO_2 photoreduction[17, 38]. In these apications, and in addition to the two most common phases of TiO_2, there are many nanostructured forms it can be grown in including nanospheres[39-41], nanotubes[42-44], nanowires[32, 45, 46], and nanorods[47-49]. These nanostructures are grown with a variety of methods and steps, which include electrochemical anodization, hydrothermal or solvothermal synthesis, high temperature annealing, sol-gel methods, porous templating, chemical vapor deposition, and atomizing spray depositions.

As a semiconductor, TiO_2 is UV sensitive, and strongly absorbs light up to about 400 nm wavelength[50], with some absorption in the visible spectrum due to impurities or

dopants[51]. It is an *n*-type semiconductor in bulk due to the formation of oxygen vacancies and titanium interstitial defects[52]. In nanostructures the *n*-type distinction is less common because of an increasing dependence on surface defects relative to bulk defects[53]. Despite this, it is still possible and common for TiO_2 to be used as an electron transport layer; but it makes it important to understand and study its semiconductor properties as a nanostructure relative to the bulk material.

1.2.1 Introduction to Charge Transport in Nanostructured TiO_2

Bulk TiO_2 is a wide bandgap semiconductor. Due to the high permittivity and low conductivity in undoped TiO_2, titania behaves as a relaxation-type semiconductor instead of a lifetime semiconductor[54]. The dielectric relaxation time in TiO_2 is large thus causing charge density fluctuations to persist over longer time periods than in typical semiconductors such as Si and GaAs, and resulting in effects such as persistent photoconductivity and space charge limited currents[55]. Another unusual attribute of TiO_2 owing partly to relaxation effects, is the wide variability over seven orders of magnitude in charge transport parameters (i.e. electron mobility) depending on the phase, method of synthesis, grain size, surface treatment, etc[56, 57]. The measured mobility is also dependent on the type of technique used to make the measurement. High frequency techniques such as time domain terahertz spectroscopy and time-resolved microwave conductivity measure charge transport over short distances (e.g. *intra*-grain transport) and may not reflect the conditions of transport most relevant to the performance of devices such as chemiresistive sensors, solar cells or photoelectrochemical cells[56]. Low frequency

methods such as impedance spectroscopy[58] and intensity modulated photocurrent/photovoltage spectroscopies[59] are more relevant to the physical conditions present in common optoelectronic devices that use TiO_2 thin films, but do not provide explicit values for the electron mobility. Other common methods like the Hall Effect cannot be used with conductive substrates, which TiO_2 nanostructures are commonly grown on. For these reasons, the charge dynamics of TiO_2 nanostructures is not extensively studied. The bulk mobility of single crystal anatase TiO_2 is reported as 4-20 $cm^2V^{-1}s^{-1}$ [60], however, the electron mobility in polycystalline nanoparticulate thin films with high trap densities and a random walk-type transport mechanism can be as low as 10^{-7} $cm^2V^{-1}s^{-1}$ [61]. The bulk mobility of single crystal rutile TiO_2 is about 0.1 $cm^2V^{-1}s^{-1}$ [62] but can be much lower due to the same problems.

As the dimensions of a wire or film or structure decrease, the object's size and surfaces begin to have a greater effect on the optical, electrical, and mechanical properties. This can be due to a number of effects; for very small nanostructures of many materials, on the order of 10 nm or less, quantum effects begin to occur such as tunneling or bandgap shifts. The exciton Bohr radius of TiO_2 smaller than 2 nm[63, 64]. Therefore, classic quantum confinement effects are not seen in TiO_2 nanostructures. However the increased effect of the surface and the ambient does manifest itself in the conductivity, absorption and luminescence of nanometer-sized TiO_2. For larger size dimensions (~100 nm – 1 μm), but not quite on the order of bulk material, different effects can occur which affect the conductivity as well, including a relative increase of surface effects, grain sizes, charge

carrier path length differences, Mie scattering, and material differences due to nano- or microfabrication.

1.2.2 Introduction to the Optical Properties of TiO_2 Nanostructures

As previously mentioned, TiO_2 is a large bandgap semiconductor, which makes them useful as UV blocking agents in sunscreens or as UV detectors or sensors. Anatase has an indirect band gap while rutile has a direct band gap where the conduction band and valence band align over the Γ plane[28], though neither commonly exhibit strong photoluminescence. Theory predicts the formation of 2D excitons in both anatase and rutile. It is only extremely recently that strongly bound 2D excitons with character intermediate between Frenkel- and Wannier- excitons have been observed in anatase single crystals and nanoparticles[65]. Due to the large bandgap, TiO_2 is mostly transparent in the visible spectrum. This gives flexibility in the use of dyes, quantum dots, biomarkers, or other light sensitive materials when making devices or conducting experiments – the TiO_2 can often act as a scaffold for visible light sensors and photocatalysts while not absorbing visible light itself[66, 67]. This can be incorporated with the methods of sputtering[17], electrodeposition[68], photodeposition[69], spin or drop coating[48], or Succesive Ionic Layer Adsorption and Reaction (SILAR)[70] to name a few.

Using the methods above, a UV sensor using TiO_2, nanostructured or otherwise, can be made into a visible light sensor, so long as the introduced material is sufficiently absorbing

and the charge transfer between device and detector is still high enough to be measured. For these sensing purposes, a TiO_2 scaffold also has an added benefit because TiO_2 nanostructures are highly dispersive, and can increase the path length of any light passing through them via reflection, refraction, and diffraction[71, 72]. This is why TiO_2 nanotubes and nanowires often appear cloudy (Figure 2) instead of completely transparent, despite no visible light being absorbed.

Figure 2: Rutile TiO_2 Nanowires (the white opaque region) grown on an FTO slide

1.3 Introduction to Charge Carrier Dynamics

One of the most important topics in modern electrical engineering is knowing how charges move through a material or across heterojunctions. Since the arrival of the diode, charge transport and charge transfer problems are no longer solved by linear application of Ohm's law. Integrated circuits, which make up a huge portion of the electronics industry, are made of semiconductors; as are LED's, solar cells, and many chemical and light sensors.

To model these semiconductors and to discover how charge moves through them, we need to know a lot of details about the material itself; such as its crystallinity, doping concentration, defects (density and type), and the morphology and structure of the material itself. We also have to know about the charges moving through it, whether they are electrons, holes, ions, or a mix; whether they were generated by injection, light, or heat; and whether it is a strong or weak signal; or a high or low frequency signal. Due to the large number of parameters involved, our goals in characterizing charge transport will be simplified to dealing with TiO_2 nanostructures and a test of recently synthesized tellurophenes provided by the Rivard group in the Chemistry Department.

Most materials' charge carrier dynamics can be approximated by a few key material parameters. Conductivity (σ) is a measure of how much current (J) flows relative to an applied electric field (E). Conductivity is typically viewed as a sum of electron conductivity and hole conductivity which can in turn be broken up as the product of mobility (μ) and the mobile charge density (n).

$$\vec{J} = \sigma \vec{E} \quad (1)$$

$$\sigma = q n_e \mu_e + q n_h \mu_h \quad (2)$$

Other considerations for measuring the current include what 'regime' the material is conducting within. The Ohmic regime assumes that charge carriers are moving through the material without accumulating in traps or reaching contact barriers. This type of transport occurs when the excess charge carrier concentration does not exceed the

equilibrium or steady-state carrier concentration. For non-metallic materials, particularly wide bandgap semiconductors and insulators, the equilibrium carrier concentration can be quite low so that even small excess charge concentrations can be large relative to the equilibrium carriers. When this happens, the material conducts in the space-charge limited current (SCLC) regime[73, 74]. Essentially, the current is no longer limited by how many equilibrium charge carriers can be moved by the electric field; the current now primarily consists of excited or injected carriers. The main limiting factor in current flow at this point is the space charge that forms near the source of the excess carriers, acting as a barrier for further charges to be injected or excited[75, 76].

1.4 Introduction to Self-Assembled Monolayers and Charge Transfer Applications

Self-Assembled Monolayers (SAMs) are common in research across many fields because they act as extremely thin coatings which can greatly change the properties of a material surface. They are easy to work with because they self-assemble, and the method of preparation is often as simple as setting up a suitable environment for growth.

SAMs are of interest in research today because they can give us insights on self-organization, surface energy modification, and they can accurately model 2D problems in physical chemistry and statistical physics[77]. SAMs are also very useful because they have applications in many fields; including amphiphobic coatings[78, 79], corrosion

protection[80, 81], biosensing and biomedical implants[82, 83], molecular sensing[84], work function modification[85, 86], and surface adhesion[87, 88].

SAMs are also useful to improve the electrical conduction of nanostructures such as nanotubes[79, 89], nanowires[90, 91], and nanoparticles[92]. By adsorbing to the nanostructure surface, defects along the surface can be passivated[93]. Surface problems such as a high defect density or Fermi level pinning can be fixed using SAMs in this way. A lower defect density would improve current movement along the surface of the nanostructures and reduce the rate of unwanted recombination when used in devices like LED's or solar cells. Removing or adjusting the effect of Fermi level pinning could also improve surface interfaces with other electrical layers in the device by improving energy level matching, or reduce the trap density for charge carriers at the surface, which would also improve mobility of the materials[94, 95].

SAMs are most commonly organic molecules with two key functional groups, a head group that will chemically adsorb to the surface, and a tail group that will give rise to the modified surface properties[77]. The head group is chosen to strongly adhere to the desired surface, to ensure stability of the monolayer and to speed up the adsorption process. The tail group is often a rod-like organic molecule with two key properties. First, the tail group should not bond to the head group to ensure that the growth stops after the first layer has covered the surface. Second, the tail group should not be too large so that it can accommodate close-packing of the head groups on the surface, enabling complete and uniform surface

coverage. A tail group that is too large will not be able to form the columnar or tilted columnar structure that is necessary for successful self-assembly.

Due to their organic nature, SAMs must be chosen carefully so that they do not decrease the conductivity of the device being treated. Non π-conjugated compounds are insulating. Even π-conjugated organic molecules are generally much less conductive because they are larger molecules that do not lose their individual identity in molecular crystals (thus preventing the requisite delocalization of valence electrons)[96]. The low symmetry of molecular crystals that typically arrange themselves in monoclinic or triclinic Bravais lattices also prevents simple substitutional doping because thermodynamic and kinetic considerations decrease the probability of an electron-donating or hole-donating foreign molecule resulting in a shallow dopant energy level[97]. Therefore, a high carrier density cannot be obtained as in metals; organic molecules are also rarely crystalline, or require processing to make them crystalline – this leads to much lower mobility than their inorganic counterparts. Organic charge transport is also typically a hopping process, as charges must move past an energy barrier when moving from molecule to molecule[98]. This is typically a slower process than transport in crystalline inorganic materials, where charge carriers move through the material lattice in continuous bands. As a result of these problems with organic SAMs, it is important that charge does not transfer into the SAMs from the nanostructures, and that the SAMs only passivate the surface.

1.5 Introduction to Photoluminescence and Time Resolved Photoluminescence

The rate of spontaneous radiative recombination of excess carriers (photoluminescence lifetime) is an important characterization factor for many materials. The rate of decay of free carriers or excitons that causes this photoluminescence is mostly determined by Fermi's golden rule, shown below, which states that the transition rate of electrons from one state to another is proportional to the overlap of initial states and final states, the density of the final states, and a coupling coefficient based on how well transitions can occur between the two states (The Hamiltonian). This coupling coefficient is most important in determining transition rates, and it can be either high or low based on the nature of the initial and final states.

$$\Gamma_{i\to f} = \frac{2\pi}{\hbar} | < f|H'|i > |^2 \rho \qquad (3)$$

Where the rate, (Γ), is proportional to the magnitude of the transition operator (H') between the final (f) and initial (i) wave functions multiplied by the density of final states (ρ).

The quantum mechanical probability is highest for transitions that occur between singlet states[99], which means the excited electron maintains its original spin when in the excited state, and maintains it until returning to the ground state. Being common, these transitions have high coupling coefficients, and the transition rate is very fast. These fast decays are

called fluorescence, and typically occur on time scales of 1-100 *ns*. Fast transitions like this also make it unlikely that electrons will stay excited long enough to undergo slow transitions, so fluorescence is often a high quantum yield process whenever it is present.

On the other hand, the less common mechanism of photoluminescence is called phosphorescence. This is a process where the excited electron undergoes a spin flip and is no longer coupled with the ground state electron. This is called a triplet state and it is forbidden by quantum mechanical selection rules, but due to spin-orbit coupling and the relativistic interpretation of quantum mechanics, it is possible to occur, most commonly in molecules with heavy elements[100]. Being so slow, phosphorescence is prone to problems of efficiency, since a triplet state lifetime is typically on the order of microseconds to milliseconds, but can last up to a few hours in certain materials. Due to the long lifetime of phosphorescent materials, the triplet states can undergo unwanted transitions such as nonradiative relaxation, oxygen quenching or solution quenching, where the excited electron is transferred to a non-luminescent molecule in the environment, and no emissive decay occurs in the material.

1.6 Introduction to Tellurophenes: Characteristics and Applications

Tellurophenes are a class of compounds consisting of a benzene ring and a tellurophene ring sharing two of their carbon atoms. Due to the heavy tellurium atom, spin-orbit coupling occurs[101], leading to classically forbidden charge transfer between the singlet and triplet excited states of the molecule more commonly referred to as inter-system

crossing. This results in long-lived excited states that decay over long periods of time (μs – s). That being said, most tellurophene molecules and polytellurophene compounds are found to be non-emissive because the triplet molecules are particularly susceptible to quenching by ground state triplet oxygen molecules to form single oxygen species. Previous reports on tellurophenes have not shown luminescence in solid state materials, but a new class of compounds developed by the Rivard group in the University of Alberta[101, 102] was shown to be luminescent in powder form and further study into quantifying its luminescence for efficiency, mechanism, and stability could show promising results.

There are many other studies focused on using this class of compounds because they are solution-processable and have the potential for tunable phosphorescence, something that is often hard to control in organic electronics[103]. Furthermore, current phosphorescent OLED technology is limited by current material limitations; where triplet dopants (such as platinum octaethlylporphyrin[104] and iridium bipyridine[105]) are currently used as guest molecules in a host matrix of a singlet emitter to improve the quantum yield of electroluminescence in solid-state organic light emitting devices. However, this approach results in electrical and chemical instability over time as the triplet molecules segregate into domains and behave as deep electron traps. A phosphorescent matrix would overcome these advantages and result in triplet emitters with high quantum yields and good mobilities in thin film form. Many tellurophene compounds are also emissive in solution form, but solid state emission is nonexistent or much weaker due to aggregation-induced quenching[106].

Despite these problems, tellurophenes have relatively good charge carrier mobilities that require further investigation and fuel studies into their use as OLEDs or sensing devices. Current research is looking into capping agents that can either prevent aggregation of the molecules in solid state, or reducing oxygen quenching by altering the triplet state energies of the molecule – the latter effect also providing the benefit of further increasing the spectral range of the tellurophenes.

Chapter 2: Fabrication and Experimental Methods

2.1 Electrochemical Anodization of TiO_2 Nanotubes

Nanotubes offer a lot of benefits as testable layers in devices. They can be highly ordered, vertically aligned, with variable pores to allow for additional materials to be embedded within, thus creating a heterojunction in one step. They also have a very high surface area to volume ratio due to a high aspect ratio of the tubes and their hollow shape. Heterojunctions with promising device performance include noble metal nanoparticle-TiO_2 nanotube Schottky junctions for gas sensing and photocatalysis, Ag and Au filled nanotubes for optical metamaterials, II-VI quantum dot-sensitized TiO_2 nanotubes for photoelectrochemistry, conjugated polymer-filled TiO_2 nanotube *p*−*n* junctions for photovoltaics, and halide perovskite-filled TiO_2 nanotubes for photovoltaics and photodetectors. The most common method for fabricating TiO_2 nanotubes is electrochemical anodization[42, 44, 107, 108]. This method involves two main steps: an electrochemical oxidation of titanium to titanium dioxide, which is typically controlled by a power supply; and simultaneous etching of a preferential crystal plane in TiO_2, which requires fluoride, chloride, or perchlorate containing acids or salts such as HF, NH_4F, NaF, HCl, $HClO_4$, etc.

The method used in this work involves a plastic anodization container with a specially designed lid for holding the titanium dioxide half-submerged in the anodizing solution. The anodization solution is Ethylene Glycol (EG)-based, with 4% H_2O and 0.3% NH_4F by

mass, though variation exists in the literature. The entire setup is run in an ice bath in order to keep the temperature low and constant, because the anodizing current can often heat the solution up to high temperatures. Anodization can take between a few minutes to multiple days depending on the anodization parameters and the length of nanotubes desired. The anodizing voltage is also variable, usually between 40 to 120 V, and it is applied positively to the titanium foil, relative to a cathode that is either titanium, platinum, or graphite. The most important detail is to make sure the electric field near the nanotubes is constant. This includes the base and top of the nanotubes; and it is initially important for controlled oxidation of the titanium foil, then later important for consistent etching of the titanium dioxide into nanotube shapes based on the chemical reactions in Figure 3. To control the electric field, parafilm is used around the edges and back of the titanium foil so that the foil closely mimics a parallel-plate capacitor by reducing fringing fields along the sides and back of the samples. The temperature, water level, and distance between anode and cathode is kept consistent between all experiments. The anode and cathode are cut at specific dimensions of 1.5'' by 0.5'' and then cleaned with acetone, water, and methanol in an ultrasonic bath for 10 minutes each.

Field assisted oxidation:

$$Ti + 2H_2O \rightarrow TiO_2 + 4H^+ + 4e^-$$

Field assisted migration:

$$Ti \rightarrow Ti^{4+} + 4e^-$$

Field assisted dissolution:

$$TiO_2 + 6F^- + 4H^+ \rightarrow [TiF_6]^{2-} + 2H_2O$$

Chemical dissolution:

$$TiO_2 + 6HF \rightarrow [TiF_6]^{2-} + 2H_2O + 2H^+$$

Figure 3: The anodization reactions that govern TiO_2 nanotube growth.

With the proper setup and reaction conditions, the process begins with a constant voltage and initially a high current because the bare titanium foil is so easily oxidized to TiO_2. As the TiO_2 layer thickens with time, current decreases quickly due to increased resistance from the growing oxide layer. The current will then begin to plateau as the barrier layer growth slows, and then will begin to reach an equilibrium barrier layer thickness as the TiO_2 is etched away, leaving pores that aid the flow of ions toward the titanium sheet underneath. The pores continue to grow deeper into the TiO_2 layer because that is where the electric field is highest, and the path for ions and electrons faces the least resistance. The end result is vertically oriented, highly uniform TiO_2 nanotubes completely covering the original titanium substrate. There is also a barrier layer, usually about 50-200 *nm* thick separating the foil from the nanotubes. The nanotube walls will also be less thick at the top compared to the base; this is because the top of the nanotubes forms first, and is slightly etched over time due to the fluoride-based solution. Depending on the anodization parameters, these nanotubes might be loosely attached to the original substrate, in which case they can be delaminated without extensive damage to the structure[109]. This delamination results in a nanotube layer that is fully detached from the substrate, and depending on the thickness it can be very fragile, but also very useful for sensing applications where the titanium substrate would hinder application.

The nanotubes grown this way are amorphous (and insulating), so an annealing step is needed to bring them to a polycrystalline anatase phase (which is semiconducting). The nanotubes are annealed at 450 ºC for 2 hours with a 10 sccm oxygen flow, to fill any

potential oxygen vacancies in the TiO_2 crystals and to achieve better charge mobility through the nanotubes. This process also mechanically strengthens the nanotube structure, which can be especially important for the fragile nanotube membranes.

2.2 Solvothermal Growth of TiO_2 Nanowires

TiO_2 nanowires are similar to nanotubes in that they are organized, vertically oriented nanostructures with flexible methods of growth allowing for variation in dimensions, shapes, and crystal phase. Nanowires differ from nanotubes in that they are not hollow and are monocrystalline as opposed to polycrystalline nanotubes. Nanowires also differ in that they are fabricated using solvothermal methods, which involves performing a chemical reaction under conditions of high temperature and pressure[110-112]. In practice, this involves heating a specific solvent containing the required precursors under specific temperature and pressure conditions in a teflon vessel to grow elemental or compound nanowires on a desired substrate. Nanowire growth is simpler in that it only involves heating a solvent above its critical point, and allowing the other agents in the solvent to grow the nanowires in a bottom-up process. This growth only takes a few hours for nanowires with a length of 1-5 microns. When the solvent is water, the growth process is called hydrothermal synthesis. Hydrothermal growth leverages the changes in the solubility of ions and ionic compounds in water as the critical point is approached, in order to force precipitation of the desired compounds.

An additional benefit of the solvothermal growth technique is that it does not require any high temperature annealing afterwards to form a crystalline or polycrystalline phase. The

process itself only requires heating to 180 ºC, and the TiO_2 grows via a crystallization process that results directly in rutile phase. This is useful because it matches the phase of the conductive Fluorine-doped tin oxide (FTO) substrate and therefore strongly adheres to that surface. The downside is that using other substrates is more difficult and requires a seed layer of TiO_2, added by spin or drop coating before the solvothermal treatment begins. The solvothermal recipe typically involves three main precursors. First, a solvent that dissolves the other precursors adequately at room temperature, but with a low enough boiling point that it partially evaporates when heated allowing the precursors to precipitate or crystallize out. Second, a TiO_2 source, usually a large molecule that is weakly soluble in the solvent; with heating, the loss of the solvent to evaporation will cause the TiO_2 to crystallize along every surface covered by the solution. Fortunately this process is preferential to crystallization on the FTO substrate because of the matching crystal phases and proximal lattice parameters (rutile: a = 0.4594, c = 0.2958, and FTO: a = 0.4737, c = 0.3185 nm)[113]. Third, a capping agent or stabilizing agent is required to grow nanotubes of specific dimensions and spacings. The capping agent inhibits growth in certain crystal phases or orientations, resulting in the 1D growth we see for nanowires. Since the process is essentially due to random nucleation of the nanowires on the FTO surface, it is difficult to control once started; however, we can selectively etch the FTO beforehand on a macro-, micro-, or nano- scale. This pre-etching only allows nanowires to grow on the un-etched sections of FTO, allowing us to engineer patterns or designs of nanowires on the substrate.

Our solvothermal recipe uses water as the solvent, making it a hydrothermal process. The titanium precursor is titanium butoxide, a large and highly reactive organic molecule which

acts as a titanium and oxygen source in the reaction; it is shown in Figure 4. HCl is also used as an additive to fix the pH to a low values, this ensures that the titanium precursor dissolves readily but does not lyse, react, or decompose before the growth begins. The HCl is also used for aligning the nanowires, inhibiting growth along the sidewalls of the TiO_2 due to the selective adsorption of Cl^- ions on the [110] family of surfaces, thus allowing growth only in the [001] direction. An additional precursor, acetic acid is also used for controlling the growth: acetic acid is a capping agent that enables control of the nanowire size through its adsorption on to TiO_2 surfaces, and also prevents the titanium dioxide from crystallizing on the sidewalls of the Teflon container, which results in a more dense growth of nanowires on the desired substrate.

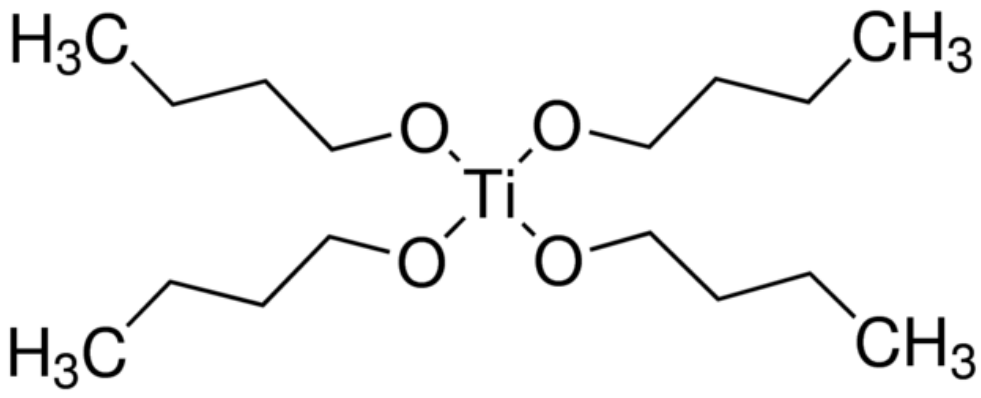

Figure 4: The chemical structure of titanium butoxide

The growth recipe consists of 100 µL of titanium butoxide (99% Sigma Aldrich) dissolved in 5 mL deionized H_2O, 2.5 mL acetic acid (99% Fisher Scientific), and 2.5 mL HCl (99% Fisher Scientific). This is put in a teflon reaction vessel and a PARR reaction bomb heated in an oven to 180 ºC. The cleaned FTO substrate is placed at an angle against the wall,

conductive side down. The growth begins when the solution begins to heat above its boiling point, the amount of liquid solvent decreases, and the titanium precursor will hydrolyze at the FTO surface, leaving TiO_2 nucleation sites behind. Because these nucleation sites have the rutile phase, further growth is preferential at these locations. Combined with the acetic acid and HCl which control the growth orientation, nanowires will continue to grow until they are removed from the solution or the temperature is lowered. This growth occurs over 4 hours and afterwards the solution is cooled under flowing water, the nanowire substrates are removed and cleaned with methanol and dried under nitrogen. Longer growth is possible but the glass substrate begins to lose its transparency if left too long in the growth solution due to the extreme conditions.

The resulting nanowires are 1.5-2 μm in length and 40-50 nm in diameter. The nanowires are individual rutile single crystals (as shown by X-ray Diffraction(XRD) and Transmission Electron Microscopy (TEM)) with a square cross section as shown in Figure 5. The rutile TiO_2 nanowires are characterized with XRD and Ultraviolet-Visible spectroscopy (UV-Vis) to ensure quality before any tests are done; the results of a typical characterization are shown in Figure 6.

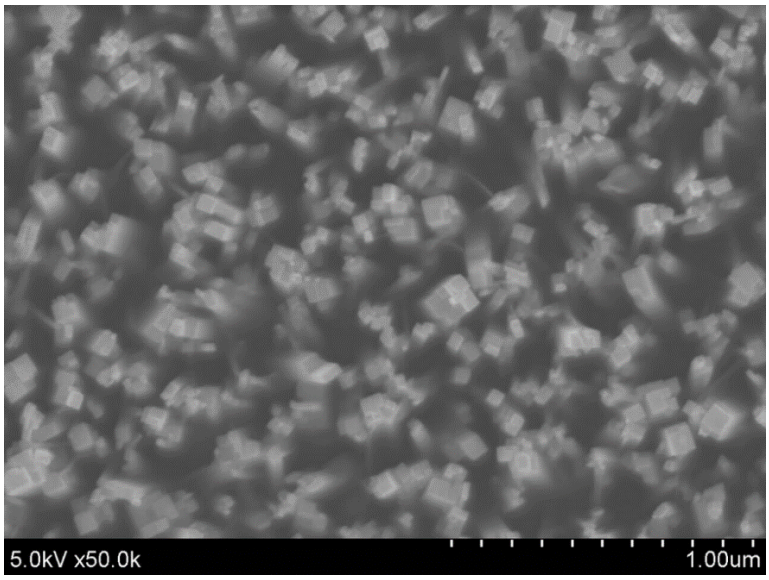

Figure 5: Rutile single crystal nanowires

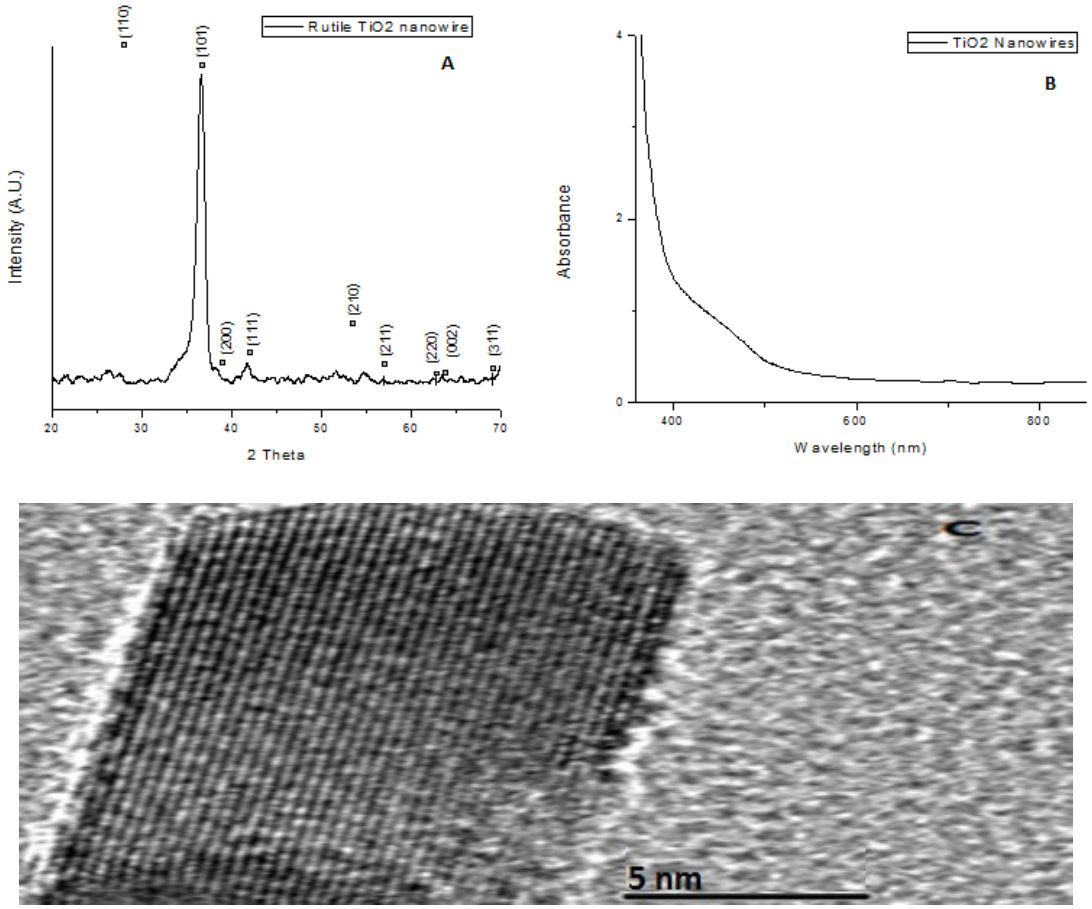

Figure 6: XRD (A), UV-Vis (B), and TEM (C) of single crystal rutile nanowires

2.3 Formation of Self Assembled Monolayers

The addition of SAMs is often done to change the surface energy of a material. This work was originally done on tuning the wettability of surfaces; where different perfluorinated compounds were used to lower the surface energy of titanium nanotube arrays, resulting in amphiphobic surfaces that are repellent to both water and organic solvents[79]. The methods used are adapted from that work.

The SAMs were grown on TiO_2 nanowire substrates. First a cleaning process is done using oxygen plasma in a benchtop RIE Trion system. This clears the nanowires of debris such as hydrocarbons or surface impurities from the anodization process. The oxygen plasma also creates reactive oxygen on the surface of the TiO_2 nanowires, increasing the adsorption rate of the SAM. The oxygen plasma is formed using 50 mTorr oxygen under 250W RF power, this is applied for 10 minutes to the sample and quickly followed by application of the SAM.

Octadecylphosphonic acid (ODPA) was the chosen SAM used in our experiments. This molecule is shown in Figure 7. ODPA is a long chain alipathic hydrocarbon with a phosphonic acid head group, which is known to strongly adhere to the TiO_2 surface[114]. Surface functionalization is done by immersion of the nanowire sample in 15 mL of 1 mM solution of each of the SAMs. The SAMs are immersed for 18 hours to ensure the

monolayer is highly packed and has a low defect density, this is done at room temperature and in a sealed container. Methanol is used as the solvent because it will dissolve the amphipolar SAM molecules while still allowing them to adsorb on the surface and self-organize with few defects. Multiple studies have shown solvent choice to be important when dealing with SAM formation, and that alcohol based solvents are most often preferred[77]; we also found that water or other strongly polar solvents would disconnect the TiO_2 nanostructures from the FTO substrate.

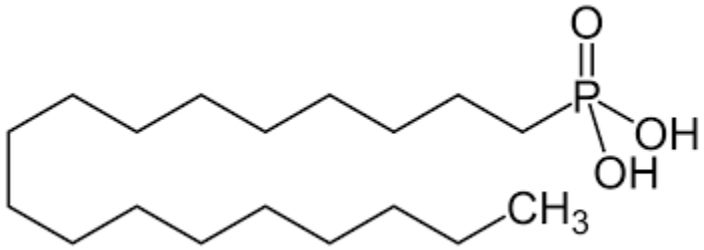

Figure 7: The ODPA molecule chosen as a passivating SAM

After the 18 h of SAM formation, the substrates would be rinsed with methanol for 5 minutes to remove any excess SAM molecules that were not adsorbed directly on the surface, then the substrates were dried under nitrogen. The substrates were tested with UV-Visible spectroscopy but due to the thinness of the monolayer and the low absorption of the organics it was identical to the bare nanowire substrate. Scanning Electron Microscopy (SEM) also showed no signs of a monolayer because the thickness is only expected to be ~ 1 nm, below the resolution limit of the machine. Fourier Transform Infrared Spectroscopy (FTIR) was done using the Diffuse Reflection Infrared Fourier Transform spectroscopy (DRIFTS) technique, which involves scratching off the nanowires into a powder and measuring their infrared reflection against a background of KBr powder.

This method destroys the sample but it allows us to collect spectra from many identical samples and acquire a lot of SAM-treated nanowire powder to find evidence of functionalization. DRIFTS also uses an integrating sphere to collect all the scattered infrared photons from the sample.

2.4 Carrier Dynamics: Characterization Methods

2.4.1 Time of Flight measurements

Time of flight is an optoelectronic characterization method that uses supra-bandgap light to excite charge carriers into the conduction band where they will be free to move. These carriers are created on one side of the material as a sheet of charge via a pulsed laser, and an oscilloscope connected to the other side of the material will collect them and record the transient signal.

In this time of flight experiment, a 337 nm nitrogen laser with a pulse rate of 20 Hz and a pulse duration of 4 ns was used. Photons of this wavelength are strongly absorbed by the TiO_2 nanowire samples which is important to the Time of Flight (TOF) setup shown in Figure 8.

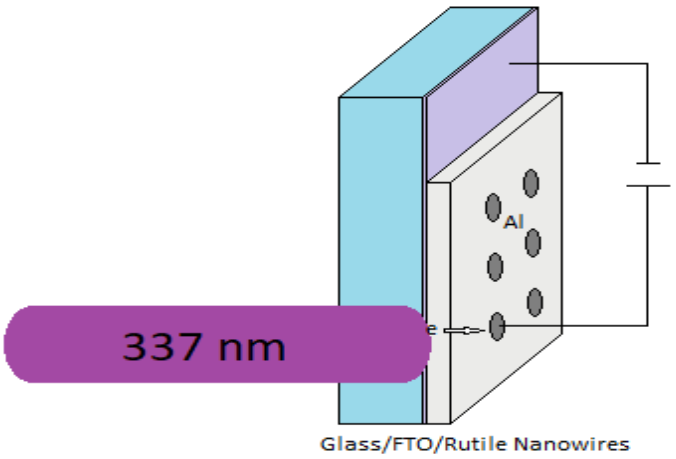

Figure 8: The TOF setup used in our experiments, the oscilloscope measures at the gold contacts. [115]

Light from the pulsed laser is illuminated on the sample from the FTO back side, it passes through to the TiO_2 nanostructures and is absorbed within the first 50-100 nm. At the top of the nanostructures, on the front side of the sample, 200 nm of metal contact is deposited. This metal is usually gold or aluminum which will form a uniform contact and collect the charges. Gold is preferred due to its ability to consistently form a blocking contact which is needed in order to ensure that excess carriers are not injected electrically from the top contact while the sheet of charge is transiting through the nanowires. The layer is deposited using e-beam evaporation, which is done at an angle to prevent gold from depositing to the base of the nanostructures and causing a short. The thickness of this layer also helps when connecting the contacts because it can protect the sample and prevent unwanted short circuits due to pressure by the contact.

As the sample is illuminated by the light pulse and photogenerated charges move through the material, a constant voltage is applied and they are collected from the metal contacts and the transient photocurrent signal is read by an oscilloscope across a variable resistor. TOF measurements can be performed either in small signal mode (wherein low level injection conditions prevail) or in large signal mode (wherein high level injection is present). The transient voltage vs. time information is recorded from this data and a typical small signal TOF plot will look like Figure 9.

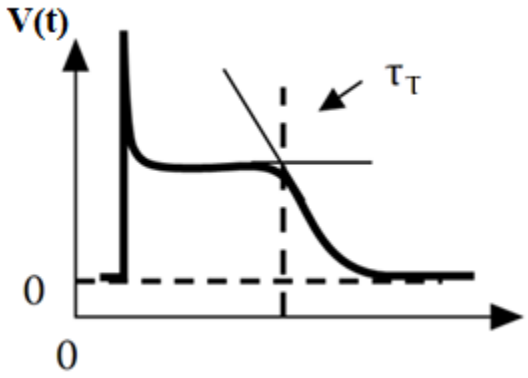

Figure 9: A typical plot of a TOF signal showing the transient voltage and with the transit time labelled. [116]

The most important parameter is called the transit time, τ_t, which is the average time it takes for actual charges to move across the sample. This transforms charge transport into a kinematics problem, and by simplifying the system to a velocity-distance problem, we can use equations 4, 5, and 6 to calculate the drift mobility directly.

$$v = \frac{d}{t} \qquad (4)$$

Since velocity is determined by the mobility of the material and the applied field, we can write this as;

$$\mu E = \frac{d}{t} \tag{5}$$

Since our material is uniform from top to bottom, the field is constant, leading to;

$$\mu = \frac{d^2}{Vt} \tag{6}$$

Thus by finding the transit time accurately, and knowing the applied voltage and the distance (thickness of our nanostructures), the drift mobility can be directly measured for many materials. This method is useful but there are many limitations on what can be measured, and it is necessary to have good control over the length and doping of the nanostructures.

The limitations arise because there are other transient signals in the system and their effect must be kept separate from the transiting charge carriers[117]. The lower limit is due to the inherent capacitance and resistance in the system. A resistor across the oscilloscope is necessary to read the current as a voltage, there is also contact resistance at the metal-nanowire junction. Also, because the sample is often quite densely populated by traps which can store charges, there is a non-zero capacitance as well. The inherent capacitance of the material and any depletion capacitance due to the blocking contact are other non-negligible capacitances in the system. That means the circuit will act like an R-C circuit when a signal is applied: the charges will collect in the sample, filling some of the traps and reaching a dynamic equilibrium, but due to the non-zero resistance this will not happen

instantaneously so there is an RC time constant, $\tau = RC$. It is important that this process occurs much faster than the transit time, so that while charges are transiting the material has already had time to reach steady state. The aforementioned capacitances are typically in series due to which the smallest capacitance dominates the system response. It is also necessary that the laser pulse duration is shorter than the transit time, to ensure the charges are closely packed and similar to an ideal sheet of charge as they move through the material, and an accurate transit time can be measured.

Time of flight measurements also have an upper limit, the transit time cannot be so slow that the excited charge pulse disperses too much or that dielectric relaxation in the semiconductor eliminates the electric field perturbation due to the injected pulse of photogenerated charge carriers. A dispersed signal would be broad, and the transit time (characterized by a sharp peak in the voltage) would not be visible. This broadening effect is due to diffusion of the charge carriers. The time it takes for the electric field perturbation to be eliminated is characterized by a dielectric relaxation time, τ_d. The dielectric relaxation is a well-known effect in all electronics, and is defined by the expression;

$$\tau_d = \frac{\varepsilon}{\sigma} \qquad (7)$$

Where ε is the real permittivity of the material and σ is the conductivity.

Fortunately, because the materials dealt with are conjugated organic molecules or wide bandgap semiconductors, their conductivity is often quite low, and the transit time is comfortably smaller than the dielectric relaxation time. Due to the relatively low carrier

mobilities in these materials, any charge dispersion that occurs due to diffusion is not fast enough to have an effect on the results.

2.4.2 Conductance, Capacitance, and Voltage measurements

Before measuring time of flight, the Current-Voltage (IV) curves, the Photocurrent-Voltage curves a.k.a photoconductivity (PC) and Capacitance-Voltage (CV) curves are measured for our material. This is done with a Keithley 4200-SCS Semiconductor Parameter Analyzer. These tests show if the sample fabrication was successful, or if there are short or open circuits due to deposition or growth problems. The IV curve will show whether our material is conducting in the Ohmic, trap-filling, or space-charge limited current (SCLC) regime. In the Ohmic regime, current follows the well-known trend of equation 2. In the space-charge limited current regime, current becomes proportional to voltage squared shown in the equation below[76];

$$J = \frac{9\varepsilon\varepsilon_0\mu V^2}{8d^3} \tag{8}$$

This equation arises in the SCLC regime because the field is no longer constant in the material because of the non-negligible presence of excess charge carriers (assumed to be unipolar). It is useful to identify an SCLC response in the material, and the voltage that induces it because it can help characterize the types of traps and their density in the material. It is also needed to help with time of flight calculations whenever the voltage applied brings the material to exhibit an SCLC response. When an SCLC regime is clearly

evident in the IV characteristic, the drift mobility may be directly estimated using Eqn (9) and can be used to verify the estimate from TOF measurements.

The PC measurement method can be used to find the mobility-lifetime product, μτ, of the material, which is a key parameter related to how long excited charges exist in an excited state, and how much current they conduct during their lifetime. This is done by measuring the IV of a material under dark conditions, then again while the sample is under continuous UV illumination to excite charge carriers. The difference in conductivity recorded is due to an increase of charge carriers in the latter situation. A large change in conductivity can be due to either a large mobility of the excess carriers, or a long lifetime (and subsequently lots of excess carriers existing). This can be derived quickly by allowing the system to reach steady-state, where the charge generation rate equals the charge recombination rate;

$$\text{Rate of photons absorbed} = \frac{\eta \mathrm{IA}}{h\upsilon} = \frac{n-n_0}{\tau} = \text{Rate of charge carriers recombined} \quad (9)$$

Where I is the intensity of the incident laser and A is the area of illumination, ν is the frequency of the incident photons, and τ is the recombination time of charge carriers in the material.

The excess charge carriers ($n-n_o$) are proportional to the change in conductivity based on equation 2, giving us;

$$\frac{\eta \mathrm{IA}}{h\upsilon} = \frac{\sigma-\sigma_0}{q\mu\tau} \quad (10)$$

Leading to;

$$\mu\tau = \frac{qh\upsilon}{\eta IA(\Delta\sigma)} \tag{11}$$

Combined with time of flight which gives us the drift mobility directly, a recombination lifetime of the charge carriers in our material can be calculated. This can also be compared with a transient photoconductivity measurement (applying a continuous voltage while switching the sample environment between illumination and darkness) which can give the recombination lifetime directly based on the fact that excess charges in the material decay exponentially, where the time constant is the recombination lifetime. This method is quick and useful but requires the lifetime to be quite long, above microseconds, in order to be detected and measured using the Keithley; otherwise other high speed measurement equipment is needed. The switching between illumination and darkness must also be much faster than the lifetime, requiring high speed electronics. For this reason it is preferable to use a combination of time of flight and IV measurements to calculate these values.

Capacitance-Voltage measurements are done using the Keithley Semiconductor Parameter Analyzer as well. It is important to know the capacitance of the sample for time of flight to be able to identify the RC time constant and ensure that there is minimal overlap with the transit time for the measurements. This is done by sweeping the voltage over the same range of the TOF voltage spectrum at a frequency of 1 kHz.

2.5 Photoluminescence, Quantum Yield, and Time Resolved Photoluminescence

2.5.1 Fabrication of Photoluminescent Tellurophenes

Phosphorescent tellurophenes were made by the Rivard group at the University of Alberta. This was done for a study on their photoluminescent properties and later their conductive properties as a thin film, and the results will be discussed later in chapter X.

The tellurophenes are a benzene ring and a tellurophene ring that share two carbon atoms. Their synthesis starts with the removal of a phenyl group from Cp_2ZrPh_2, leading to a benzozirconocene, where the zirconium can be substituted with a tellurium atom using a bipyridine substitution ($TeCl_2$)[101, 102]. The resulting tellurophene has two active sites where additional functional groups can be added, the choice of functional group can determine the photoluminescence of the compound; this study used phenyl groups and pinacolboronate (Bpin) groups. The synthesis is illustrated in Figure 10.

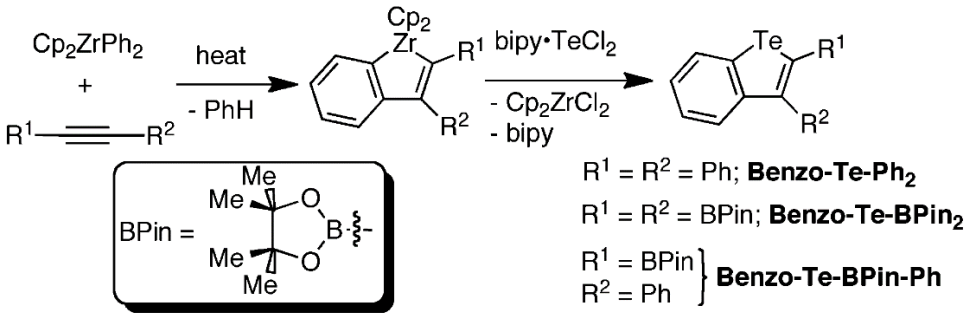

Figure 10: Synthesis done by the Rivard group to create the Tellurophenes we tested[102]

2.5.2 Measuring Photoluminescence and Recognizing Unwanted Scattering

Photoluminescence of materials is commonly measured to gather information on their light emission properties and underlying carrier dynamics. For most materials with a direct band gap, this can give information on the band gap energy and for some materials, information on any excitons generated in the material.

Photoluminescence measurements are done by exciting a material with an excitation beam or excitation wavelength. Monochromatic illumination from a continuous wave (CW) laser is sometimes used. More commonly, a broad spectrum light source such as a Xe arc lamp is coupled with a programmable monochromator with tunable slit widths to select the excitation wavelength window of interest. At the same time, a detector is present near the material and will collect an emission spectrum from the sample. The alternative can also be measured, where a specific emission is collected; and a scan of excitation wavelengths is recorded to see which produces the most desired emission. A Cary Eclipse spectrofluorometer system measured and recorded the intensities of the emission and excitation wavelengths. For these measurements, fibre optic cables were used as sources and collectors for the excitation and emission wavelengths respectively, they were connected with a special module allowing their use. The fibre optic cables allow freedom to adjust the incident and collecting angle of the light, helping to avoid unwanted specular reflection being incorrectly measured by the machine as emission from the sample.

Common physical phenomena that can make the results of photoluminescence measurements inaccurate are Raman scattering and particularly strong Mie scattering, and is so often seen in these measurements that it should be explained. A simple method for recognizing scattering and reducing the effect of unwanted scattering will also be described. Scattering, unlike photoluminescence, does not require a photon with specific energy to excite an electron to a higher energy state. Scattering, involves an electron in the material being excited to a virtual energy state that is short lived, and not based on the real band structure of the material[118]. As this electron decays, it normally decays to the same energy level it was at originally, and this is just normal reflection. Sometimes; however, the electron will decay to a higher state than it started, such as a higher energy vibrational or rotational state. When this happens, the photon re-emitted by the decay process has a different energy than the original photon (the scattering is therefore inelastic), exactly equal to the difference between the original state and the higher vibrational/rotational state. This can happen regardless of the excitation wavelength, but the difference in energy will always be constant. Scattering peaks are often sharper than photoluminescence peaks because they are based on the width of the excitation source, which is quite sharp. In order to avoid confusing scattering as photoluminescence, multiple scans should be done with slightly offset excitation wavelengths of 10-15 nm. Any scattering peaks will be offset by approximately the same amount depending on the excitation, whereas real photoluminescence peaks will be at a consistent location, because they are based on electronic decays between real electronic states, as long as the excitation wavelength is sufficiently absorbed.

2.5.3 Measuring Quantum Yield for Photoluminescent Materials

More detailed tests can be done to measure the quantum yield of the material, which is defined as the ratio of photons emitted to photons absorbed. This requires accurate knowledge of the light source intensity which was not known to us or the machine owner. However we were able to measure the light source intensity using an integrating sphere and the machine's own calibrated photodetector. The integrating sphere is a hollow spherical object with a highly reflective white coating completely covering the inside. The sphere has two adjustable openings, one for incoming light, and one for outgoing light, we only used one opening and closed the other because the optical fibres could fit together in one. Normally if the emission wavelength spectrum crosses over the excitation wavelength in a highly reflective environment, the excitation wavelength will be interpreted by the machine as emission, and the machine will reach intensity saturation. To avoid this it is necessary to use the lowest gain settings and smallest slit widths in order to record the entire intensity spectrum and integrate it over the wavelength to find the total photon count of our excitation beam. To measure the total photon count of our emission, the methods of Friend *et al*. can be used[119, 120]. This method accounts for unwanted reabsorption of the emitted or scattered light back into the sample or substrate. The equation for quantum yield is shown below;

$$\Phi = \frac{P_c - (1-A)P_b}{L_a A} \qquad (12)$$

Where A is the fraction of light absorbed by the sample from the initial beam, L_a is the photon count of the emission beam, P_c is the emitted photon count when the beam is aligned to hit the sample in the integrating sphere, and P_b is the emitted photon count when the beam is not aligned with the sample, but the sample is still in the integrating sphere. The quantum yield is an important parameter because it is a huge factor in determining whether the material can be used efficiently in LEDs or OLEDs, or as a photoluminescent marker material.

2.5.4 Measuring Time-Resolved Photoluminescence

Measuring time-resolved photoluminescence utilizes the same principles as regular photoluminescence tests. A light source is used to excite electrons in the material, and these need to be captured and recorded along with the elapsed time. A pulsed light source is required and it is synchronized with the oscilloscope so that every laser pulse sets the time to 0. A 337 nm laser source is used because the photoluminescence is previously known to be strong at that excitation. A large diameter lens system placed close to the sample collects emitted photoluminescence from a relatively large solid angle and magnifies any and all light coming from the material towards a monochromator, which blocks all wavelengths that do not match the known photoluminescence peak. With this system properly implemented, the only light that passes through the monochromator should be photoluminescence from the sample. The monochromator is directly connected to a detector and to prevent unwanted loss of the emitted light and reduce signal noise from the environment.

To measure the fast lifetimes of photoluminescence, it is necessary to be able to track changes over the nanosecond time range. A photomultiplier tube was able to sample the intensity every 10 nanoseconds so it would be able to capture phosphorescent emission and any fluorescent emission would be noticeable. At these high speeds a very high gain is required because there is very little light to be detected during that short time, but care should be taken so that light from the environment cannot enter the detector system or it can overload and break the device. The photomultiplier tube can transfer measurements to the oscilloscope which has already been synced with the laser pulse. This way the data recorded is easily read and analyzed.

To analyze the recombination lifetime of the material, the data is fit to an exponential curve; with no limit on the number of terms if it seems like there are multiple pathways to emission (bi-exponential, tri-exponential, etc.) The samples may also have fluorescent and phosphorescent components, so it is important to record data over large and small time intervals.

2.6 Microwave Resonators and Microwave Characterization

The ring-type microwave resonators used in this section were designed by the Daneshmand group in the ECE Department at the University of Alberta. The design and simulation work done on them had been completed beforehand by Zarifi *et al*[121]. This section is

designed to introduce their use in characterizing semiconductor material properties, also known as time resolved microwave conductivity (TRMC) measurements.

The microwave resonators are microwave circuits which resonate at specific microwave frequencies. The resonances can be designed to have different frequencies, amplitudes, and quality factors. A picture of a typical planar microwave circuit used in our experiments is shown in Figure 11.

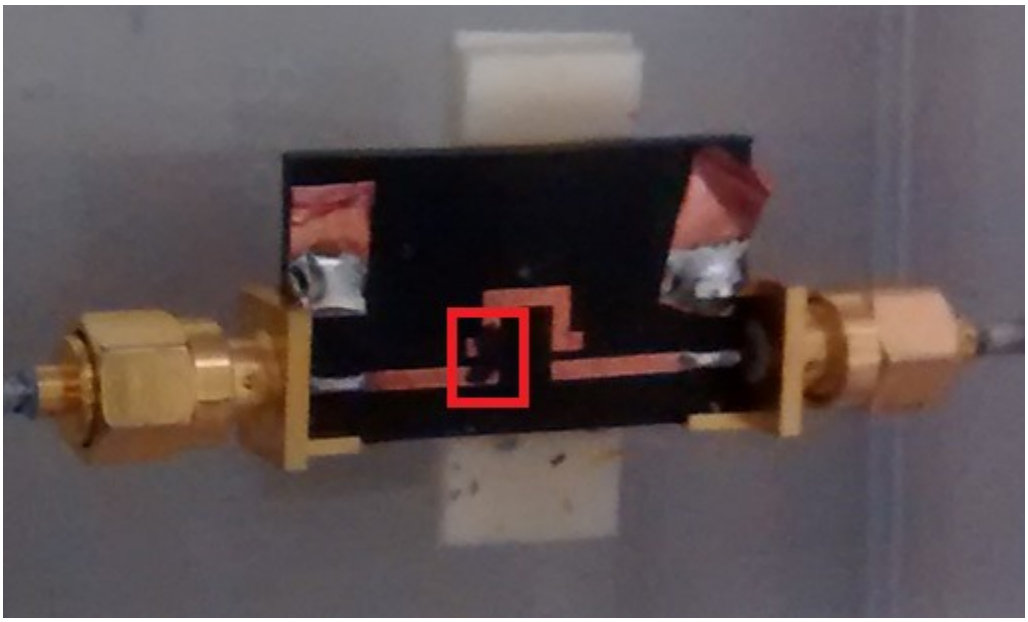

Figure 11: A microwave ring resonator, with a TiO_2 membrane across the left coupling gap circled in red.

To explain the above phenomenon, the microwave resonator should be considered as an RLC circuit, something which stores and moves current, leading to preferential frequencies of transmission. Because the microwaves are not entirely confined to the patterned metal wires, there are many pathways to consider as resistors and capacitors.

Fortunately, the ring length and width are the most important factors in determining the resonance properties of the circuit, and will determine the resonance frequency. However, the coupling gap can also act as a capacitor and store charge. Because the coupling gap closely mimics a parallel plate capacitor, it is well-studied and understood. Small changes in the coupling gap environment, especially when the resonator has a high quality factor, can result in measurable changes in the resonance frequency profile, and those changes can be interpreted to provide information on the material present in the gap. For example, a material with a high dielectric constant, ε, placed within the gap will cause the capacitance of the gap to increase based on the dielectric equation;

$$C = \frac{\varepsilon A}{d} \tag{13}$$

Just like a normal RLC circuit, this increase in the overall capacitance of the circuit will cause the time constant of the entire circuit to slow down, shifting the resonant frequency to a lower value. Additionally, the added TiO_2 membrane will provide a semiconductive pathway across the coupling gap, lowering the overall resistance of the circuit, and shifting the resonant frequency to a higher value. Depending on how other variables change such as either the Q factor or the amplitude, simulations using Advance Design System and/or ANSYS HFSS were used to extract the material properties such as permittivity and conductivity from the observed experimental data.

The microwave resonator is hooked up to a Vector Network Analyzer (VNA) and a microwave signal is sent through. The VNA can measure S-parameters (S11, S12, S21, S22) which represent the ratio of power entering at a port and being collected at a port. For

example, S21 represents the ratio of power entering from port 1 that is collected at port 2 (transmission), whereas S11 measures power entering at port 1 and being collected at port 1 (reflection). S parameters are typically measured in decibels (dB). The vector network analyzer can gives us a frequency spectrum of the chosen S parameter and a visual user interface allows us to quickly find the resonant peak we want to study.

The idea of TRMC measurements using this system comes from the fact that the VNA is able to measure an entire spectrum in about 10 milliseconds. Thus any long lived, time-dependent material changes can be detected using the microwave resonator circuit without moving or disturbing the environment. UV light excitation of TiO_2 nanotube membranes was used as the test material. The UV light excites charge carriers, which leads to a change in the complex permittivity of the membrane, and the long carrier lifetime in the TiO_2 nanostructures (mostly due to carrier trapping) causes a very slow return to equilibrium when the light is turned off. This entire cycle can be measured using the VNA, and the material parameters constantly calculated at each time interval. Similar to the TRPL measurement, the recombination lifetime of carriers can be measured by fitting the data to a multi-exponential decay curve. This means we can calculate recombination of carriers without requiring radiative recombination or emission from the sample.

The use of planar ring resonators is an upgrade over the previous technology, resonant cavity waveguides. These were larger and bulkier and harder to use than the planar resonators developed by the Daneshmand group. Tuning and making planar resonators is also easier than replacing the large parts of a cavity waveguide. The planar resonators are

also more conducive to measurements of a substrate's changing environment, whereas the cavity waveguide environment is fixed and previous research has not focused on manipulating it for purposes like gas, liquid, or humidity sensing.

Chapter 3: Experimental Results and Analysis

3.1 Charge Carrier Dynamics of Functionalized TiO_2 Nanowires

3.1.1 Experimental Setup

One of the key goals of this research project is to improve the understanding of our TiO_2 nanowires, and if possible, use them in devices such as solar cells, gas sensors, LEDs, or transistors. Previous experiments calculating the mobility of TiO_2 have been successful on the bulk material (large single crystals of rutile), but transport within nanostructures had been much less studied, and TOF had not been done. Other measurement techniques such as Hall Mobility did not work with our nanostructures because of the conductive FTO below, which acts as a secondary pathway for lateral transport. To characterize the nanowires it was necessary to measure the charge transport along the nanowire axis. Based on the initial results, we then tried to improve the nanowires' charge transport properties using SAM functionalization.

The experiment started by making multiple TiO_2 nanowire arrays using the process described in chapter 2. Fluorine doped tin oxide (FTO) was cleaned by immersion in acetone, methanol, and then water under ultrasonication. The FTO was dried with nitrogen and individually put in a solution of 5 mL H_2O, 2.5 mL HCl, 2.5 mL Acetic acid, and 200 µL titanium butoxide in a PARR reaction vessel, with the conductive FTO side facing diagonally downwards. The reaction vessel loaded with FTO was kept at 180ºC for 4 hours, then cooled in flowing water for 30 minutes and the FTO- rutile nanowire substrate was rinsed with methanol and dried under nitrogen. The nanowire array substrate was then

connected to a shadow mask with finger-like patterning and 200 nm of aluminum was deposited by e-beam deposition under high vacuum at a rate of 1.4 Å/s. A schematic of these steps is shown below in Figure 12.

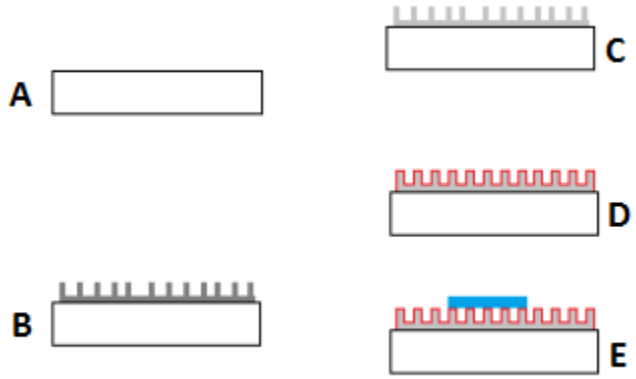

Figure 12: Schematic of nanowire growth and funcitonalization for TOF on an FTO substrate: (A) the blank FTO substrate (B) nanowires grown via hydrothermal method (C) debris removed from nanowires using oxygen plasma (D) nanowires immersed in SAM for functionalization (E) metal contact thermally evaporated onto nanowires

3.1.2 Charge Carrier Dynamics of TiO_2 Nanowires

The fabricated TiO_2 nanowire arrays were tested using IV and CV modes on the Keithley (Figure 13), including illuminated tests and optical tests, to ensure the nanowire arrays were sufficiently conductive with no fabrication defects; and that they adequately absorbed the 337 nm UV pulses that would be used for TOF tests. The penetration depth of the light was found to be about 200 nm for the rutile nanowires based on the UV-Vis data from chapter 2 and the following equation derived from the Beer-Lambert Law;

$$\delta = \frac{L}{A} \qquad (14)$$

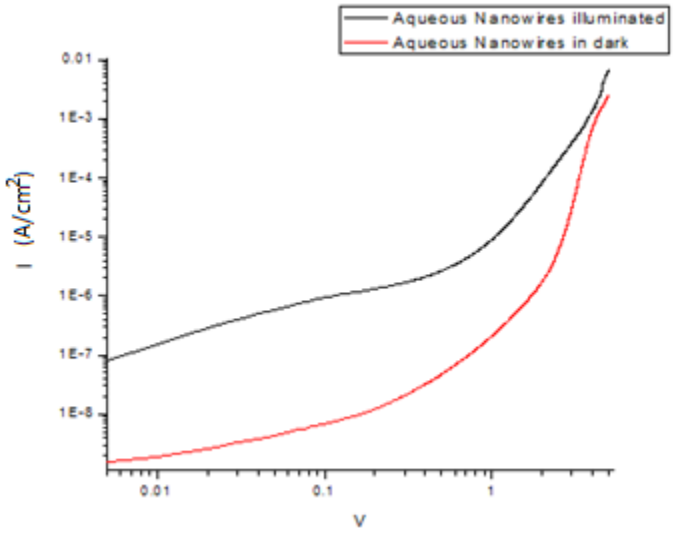

Figure 13: illuminated and dark IV measurements showing the increased photoconductivity under UV illumination, and the onset of SCLC at 3 V

Based on the IV measurements, the TiO_2 nanowire arrays are shown to follow an Ohmic, then SCLC response, separated by a sharp increase in current within the trap filling region. This implies that the nanowire arrays are heavily populated with deep traps, which can hold and keep charge carriers immobile for long time periods, lowering the conductivity greatly. We recorded the trap-free limit voltage (V_{TFL}) as the voltage where the traps are completely filled; around 3 V where the SCLC and TFL slopes overlap, this can be used to calculate the number of traps present in the nanowires, which was found using the values below;

$$N_T = \frac{2\varepsilon V_{TFL}}{eL^2} = 3.5 \times 10^{16}\ cm^{-3}$$

This is a high density of deep traps, and it means our nanostructures are very different from bulk rutile TiO_2 which has primarily shallow traps due to oxygen vacancies and Ti^{3+} interstitials. This high trap density, which typically leads to a low drift mobility, is true

despite the rutile nanowires being individual single crystals, which would lead to an expectation of a high carrier mobility.

The TOF measurement was done using the same nanowires using the setup described in section 2.3.1 with a constant 2 V sweeping voltage that pushes electrons through the material towards the aluminum contact. The data is collected and recorded using an oscilloscope and a 50 Ω resistor.

There is an initial peak at the beginning which represents the system response time, RC. We can confirm this because we know the resistance of the system to be the 50 Ω applied resistance, and the capacitance from our CV plots was 10 nF (shown in Figure 15), resulting in a system response time of 500 ns. The data shows that the system response time does not overlap or cloud the transit time, which is the lower bound for this experiment.

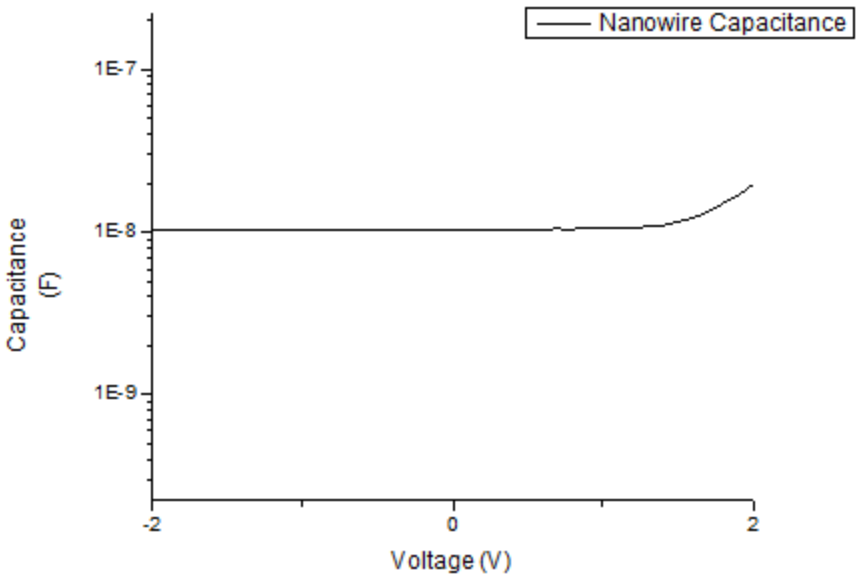

Figure 14: CV data from single crystal rutile nanowires using a voltage sweep.

Because the number of carriers generated by the incident laser pulse is larger than the equilibrium carrier concentration, large signal TOF conditions prevail, the SCLC regime is relevant and equation 6 is given a correction factor of 0.787[75]. The resulting drift mobility from that equation is $1.44 \times 10^{-5} cm^2 V^{-1} s^{-1}$, much lower than the drift mobility of bulk rutile TiO_2 which has been previously measured to be $0.1 cm^2 V^{-1} s^{-1}$. This further corroborates that the TiO_2 nanowires are highly populated by traps and defects in the crystal lattice that lower mobility.

The result of TOF tests done on TiO_2 nanowire arrays with a titanium electrode is shown in Figure 16 below;

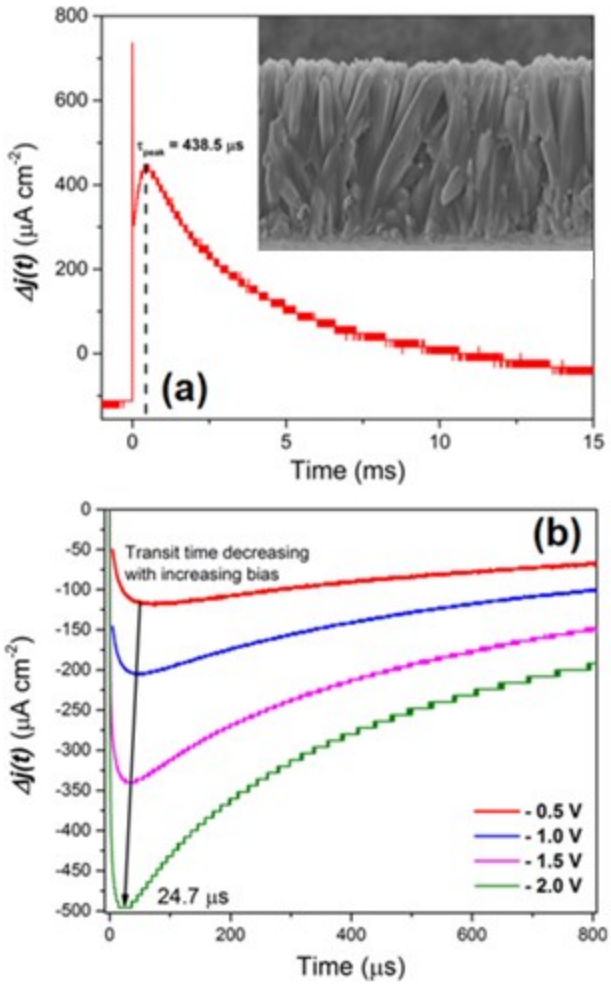

Figure 15: The TOF result of a single crystal rutile nanowire with a titanium contact, allowing for hole conduction to also be measured. [90]

The titanium electrode was used to create a better blocking contact for both electrons and holes because of its higher work function than Al. The above graph shows TOF in both polarities, sweeping electrons to the detector in A, and holes to the detector in B. The difference in polarity is due to the voltage applied to the sample, and the corresponding polarity of charge carriers measured by the oscilloscope. The multiple plots for hole transport that were obtained show the trend of increasing voltage decreasing the transit

time but the effect is not totally linear because some of the measurements occur in the SCLC regime.

The results are consistent with the earlier TOF results using an aluminum electrode. The electron drift mobility was measured to be $4.6 \times 10^{-6} cm^2 V^{-1} s^{-1}$, and the hole drift mobility was measured to be $8.2 \times 10^{-6} cm^2 V^{-1} s^{-1}$. The very low drift mobilities reported in this work still show that there are large amounts of defects affecting the nanowires.

These traps could be caused by unwanted chemical impurities arising from the fabrication process, but it is suspected that the nature of the nanostructures, with their high surface area to volume ratio, means that surface defects have a huge effect on conductive properties.

3.1.3 Charge Carrier Dynamics of Functionalized TiO_2 Nanowires

With regard to the above results, the next step was to see if the low drift mobility was a problem that could be solved. There are many ways to reduce the defect density such as improving crystallization through high temperature annealing or adding reagents to the reaction vessel to promote certain crystal orientations, but a post fabrication SAM process was used because of its simplicity, low cost, and the knowledge that it would only target the surface of the nanowires, where we expect the majority of defects to exist.

Before the SAM is added, the nanowire array undergoes an oxygen plasma cleaning process. Then an octadecylphosphonic acid (ODPA) SAM was added onto the nanowire substrate by dissolving 1 mM of ODPA in a 4:1 solution of isopropanol to water, and immersing the sample for 18 hours. This was done both pre- and post- deposition of the metal contact in case the deposition process caused the organic ODPA to overheat and break down; it was found that adding the ODPA before the metal deposition worked better to improve the drift mobility of the nanowire arrays, because with post-deposition the ODPA did not reach underneath the deposited metal to the nanowires that would be carrying current. The ODPA should align itself along the surface of the nanowires, but it is not expected to conduct itself because it is a long, unconjugated organic molecule. The ODPA can bind in multiple ways based on how to oxygen molecules orient themselves to the surface; this is known as the denticity of the molecule and is exhibited in Figure 16.

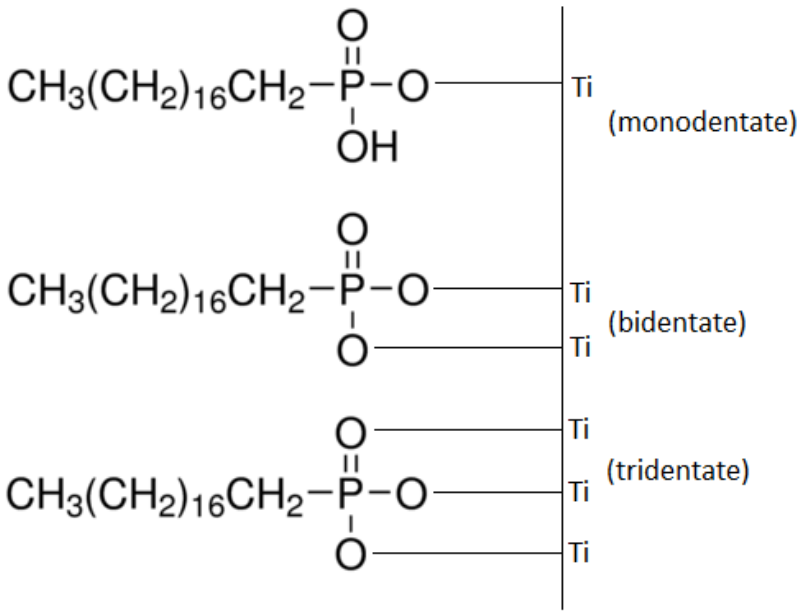

Figure 16: The different possible orientations (denticities) of ODPA on TiO_2 [122]

Characterization of the SAM was performed primarily by FTIR analysis shown in Figure 17.

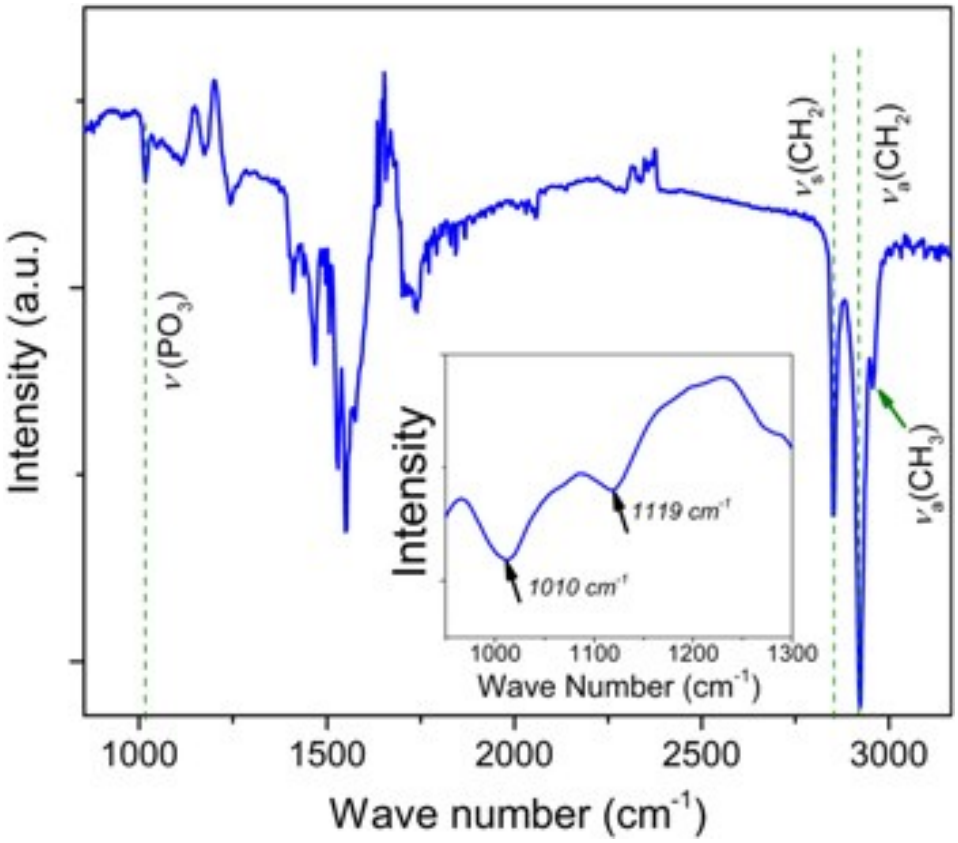

Figure 17: FTIR data using DRIFTS on ODPA-functionalized nanowire samples [90]

The FTIR data was collected in DRIFTS mode, and it shows the expected phosphonate peaks at 1010 cm^{-1} and 1119 cm^{-1}, which indicates that the ODPA is bonded to TiO_2 [123]. Unbound phosphonate peaks occur at 1075 cm^{-1} and 950 cm^{-1} but they are not seen, indicating the ODPA is completely bound to the nanowires, and no excess unbound ODPA is present[124]. The additional CH_3 symmetric and anti-symmetric peaks at 2850 cm^{-1} and 2950 cm^{-1} show the presence of the organic tail of the ODPA, and none of the peaks listed above occurred in the bare nanowire DRIFTS reading.

The benefit of the titanium metal contact on the unpassivated nanowires in figure 15 was that we could measure the transit of both electrons and holes using this configuration, since Ti exhibited superior blocking action for electrons than Al, which ensured that photogenerated holes were not completely lost to recombination with electrically injected electrons. We found this blocking effect was even more pronounced using a platinum electrode with a work function of 6.35 eV. For this reason, TOF tests using a platinum electrode were performed in order to see both electron and hole transient photo-currents, the results are shown in Figure 18 below.

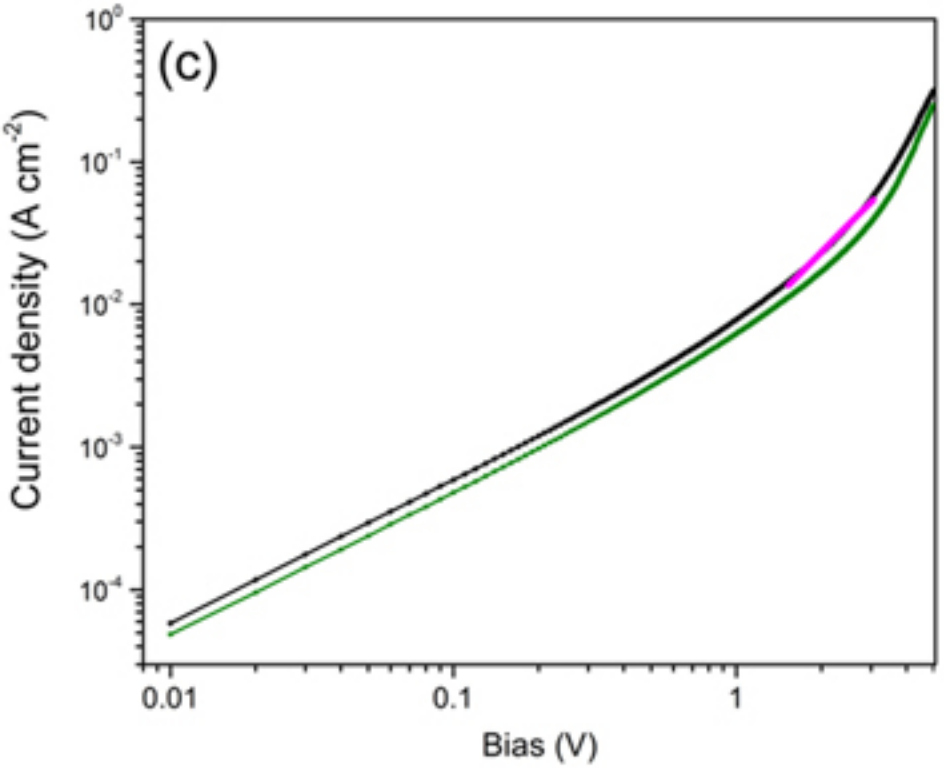

Figure 18: The IV curve for ODPA-passivated nanowires with a platinum electrode. Black represents a positive potential and green a negative potential at the Pt contact. Adapted from [90]

The IV curve for the ODPA-functionalized nanowires (Figure 17) shows an SCLC response, but does not have a trap-filling region where the current grows faster than V^2. Instead it has a smooth curve transitioning from the Ohmic regime ($J \alpha V$) to the SCLC regime ($J \alpha V^2$) This indicates that the traps are no longer high energy deep traps, but low energy shallow traps. This is indicative of the passivation of the traps. Essentially, the phosphonate head group chemisorbs to a dangling bond at the surface, eliminating the trap. In addition, the close-packed hydrophobic alkyl chains block the entry of water molecules and hydroxyl groups near the nanowire surface and thus prevent the capture of free electrons and holes by chemisorbed water and hydroxyl ions respectively. Based on the SCLC current-voltage relation (equation 8) being applied at the pink line where the SCLC regime begins; the electron and hole mobility are found to be $2.7 \times 10^{-4} cm^2 V^{-1} s^{-1}$ and $5.5 \times 10^{-3} cm^2 V^{-1} s^{-1}$, respectively, already an increase of ~100x relative to the unpassivated nanowires.

The TOF measurements done on the functionalized samples used the same procedure as the non-functionalized nanowire tests, the only difference was the switch to a platinum electrode for better blocking behavior. The results for the functionalized nanowire samples are shown in Figure 19.

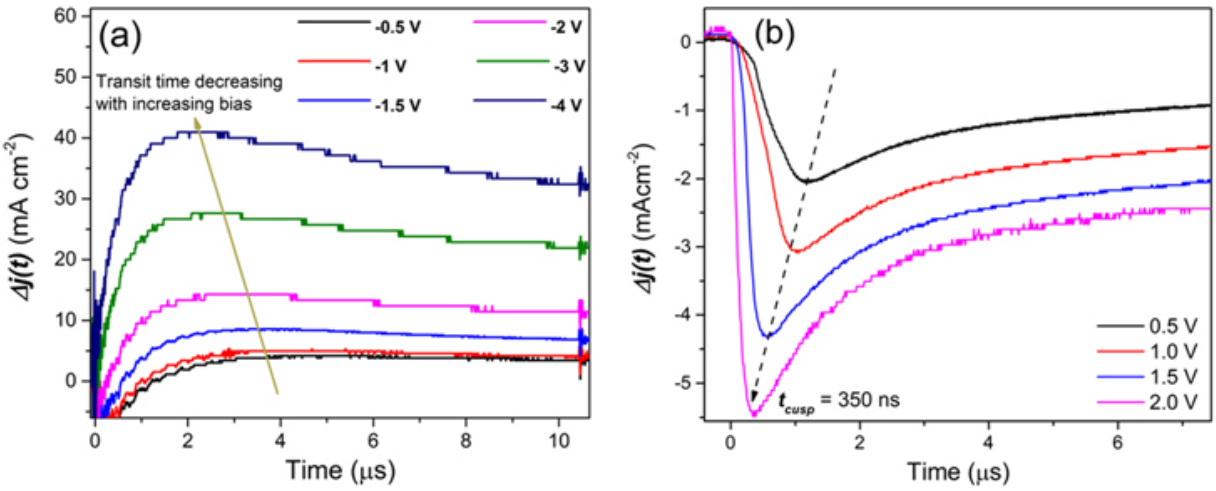

Figure 19: TOF data for electrons (a) and holes (b) for ODPA-functionalized nanowires. Adapted from [90]

The graphs show the same features as earlier TOF tests; the trend of transit time decreasing with voltage, and the sharp peak leading to a slower decay as the excess carriers trap and recombine. The hole transport peak is sharper, which suggests that the trapping of holes in ODPA-passivated rutile phase TiO_2 is less severe than that of electrons. Too much dissipation of the signal would result in the transit time being indistinguishable; and this is related to equation 5: the upper bound of TOF measurements being equal to the dielectric relaxation time. From the TOF plots in Figure 19, the electron mobility is found to be $4.3 \times 10^{-4} cm^2 V^{-1} s^{-1}$ and the hole mobility higher: $7.1 \times 10^{-3} cm^2 V^{-1} s^{-1}$, which is almost 1000x higher than when unpassivated.

3.1.4 Discussion

The charge carrier dynamics tests done in this section are useful but not commonly used measurements that can work with a wide variety of materials. The analysis of IV curves into the SCLC regime is highly necessary for materials with low equilibrium carrier concentrations, but for most commercial semiconductors like silicon and germanium, this limit is not often reached. The IV analysis to find mobility closely matches the TOF analysis in terms of result, with a maximum error of ~30% (TOF passivated electron mobility 4.3 vs IV passivated electron mobility 2.7). But this can be considered minor when dealing with huge improvements in order of magnitude. TOF is also especially useful for measuring mobility as an alternative to systems that utilize the Hall Effect; especially in devices that are multilayered, since the other layers may have undesired charge transport and the material of interest would be difficult to isolate.

More importantly, both measurement methods were decisive in showing that passivation of the nanowires using ODPA was possible and effective in reducing the number of deep traps, increasing conduction, and improving mobility of both electrons and holes. The results show that deep traps on the surface are a large factor in restricting the charge carrier mobility in TiO_2 nanowires. The extent that this can be improved by surface passivation was shown to be at least 100-1000x but there is much more room for improvement to reach the mobility of bulk TiO_2. It is unclear if the surface passivation completely nullified the effect of surface defects, or if it only passivated a portion of them. Either way, it is likely the procedure could be adapted to other devices or materials, especially nanostructured

materials such as silicon nanowires and zinc oxide thin films where surface traps are most likely to have a large effect.

The goal of continued research in this field is twofold; the first is simple: to apply passivation layers to TiO_2 nanostructures for use in solar cell devices, and the results in this chapter are already being used for that purpose. The second: to find other SAM materials that can act as passivation layers which may be better than the ODPA used here. There are many organic molecules that are candidates for passivating SAMs, and many nanostructured materials to use them on; further study could consist of simulating trap passivation or developing a model that could narrow the search.

3.2 Characterization of TiO_2 Nanostructures using Microwave Resonators

Planar microwave resonators are useful devices developed by the Daneshmand group that can give us information on a material's complex dielectric constant, even as it changes over time. We used these planar microwave resonators to measure the time-resolved microwave conductivity of our TiO_2 nanotube membranes, before and after functionalization.

3.2.1 Experimental setup

The membranes were prepared by growing TiO_2 nanotubes on titanium foil substrates. This meant cleaning the foil substrates by immersion in acetone, methanol, and then water under ultrasonic application. The anodization solution was 4% DI water, 0.3% NH_4F by mass, dispersed in ethylene glycol (EG). The foil substrates were put in the anodization solution which itself was placed in a cold water bath to maintain a constant temperature. The anodization voltage was 40 V, and the substrates were left to anodize for 72 hours without interruption. This results in amorphous nanotubes of about 160 μm in length, and 150 nm in diameter. After anodization, the nanotubes are rinsed with methanol to help delaminate the nanotubes from the foil. Then, since the nanotubes are amorphous after the anodization process, we induce crystallinity with an annealing step that keeps them at 450ºC under 15 sccm flowing oxygen to reach a crystalline anatase phase.

This gives us a titanium dioxide nanotube array membrane (TNTAM). The TNTAM is initially broken to the size of about 25 mm^2 and placed on the coupling gap of the microwave resonator while a VNA is set to constantly monitor the S21 parameter of the circuit. The microwave resonator was designed to resonate at 5.2 GHz, but this number is variable and can be changed by adjusting the ring dimensions, the placement of the TiO_2 material to the coupling gap can also change the resonance on the order of 100 MHz and it was measured at 5.078 MHz before testing began. The quality factor of the resonance peak was initially 195, a unitless quantity that describes the sharpness of the peak; mathematically it is the ratio of power stored to power lost every cycle. A high Q factor

can indicate little damping within the system, and the term is related to the overall resistance and capacitance of the circuit.

The TNTAM on the coupling gap was placed in a dark environment to prevent any unwanted excitation from room light sources, which may be caused by impurity doping of the membrane. Different UV lamps with wavelengths of 254, 365, and 405 nm were used to excite charge carriers in the membrane via absorption. A 532 nm laser light source was also used but showed no response, indicating the photon energy was not high enough to excite carriers across the TiO_2 band gap. The lamps were held at a variable distance from the TNTAMs in order to maintain a light intensity of 500 μWcm^{-2} being illuminated on the sample. The penetration depths of the different light sources were calculated by placing thinner nanotube membranes in front of a photodetector module of an oscilloscope; the intensity of the light passing through could give us the fraction of light absorbed by the material. Because light absorption follows the Beer-Lambert law, we can calculate the penetration depth using the following equation;

$$\text{Penetration depth} = \delta = \frac{-d}{\ln(\frac{I}{I_0(1-R)})} \qquad (15)$$

The penetration depth is defined as the thickness of a material required to absorb about 63% of the incident light, neglecting internal reflections. The penetration depths measured for our light sources are shown in Table 3.1.

Table 3.1: Penetration Depths of Different Laser Sources

Light Source	Penetration Depth (μm)
254 nm	0.36
365 nm	0.83
405 nm	130

This makes sense because the UV light should be strongly absorbed by the TiO_2, and based on the penetration depth it is almost completely absorbed at the surface of the membrane. The 405 nm light is on the edge of the band gap and only weakly absorbed by the TiO_2 or defects in the TiO_2 – this means that charge carriers are created almost uniformly throughout the entire thickness of the membrane. Each experiment involved illuminating the sample with one of the light sources for 10 minutes, then allowing the sample to return to equilibrium over a four hour period.

3.2.2 Microwave Characterization Results

The detailed results of the first test, illumination with the 365 nm lamp is shown in Figure 20 and 21;

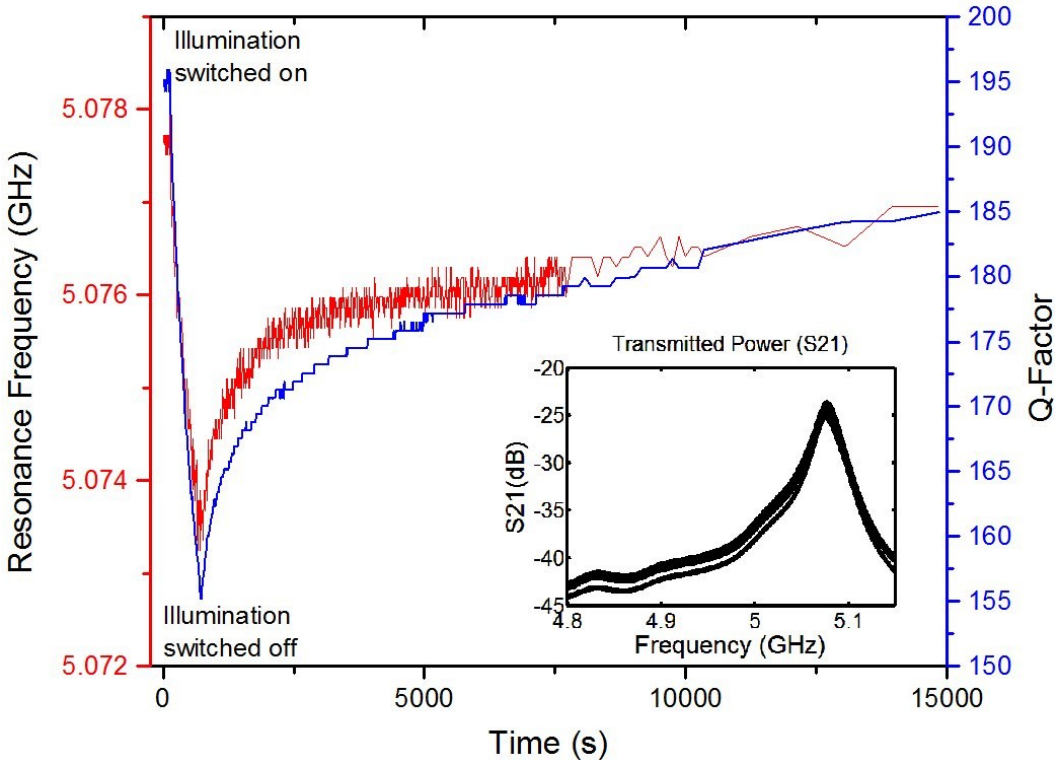

Figure 20: Time resolved data for resonance frequency and Q-factor as measured by the VNA[121]

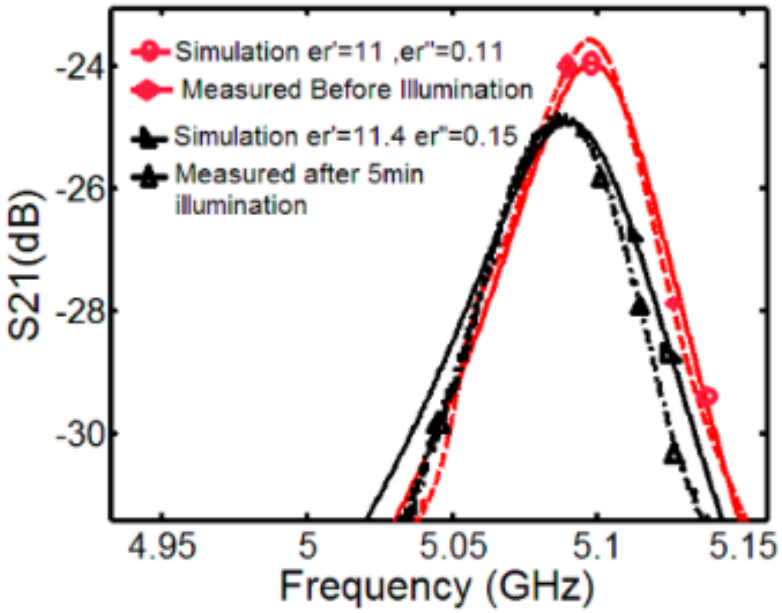

Figure 21: A zoomed in image of the small changes detectable in frequency before and after the simulation, and compared with a simulation using extracted permittivity [121]

The inset of Figure 20 shows the entire spectrum of the frequency sweep done by the VNA, before and after light illumination. Figure 21 shows the same sweep but magnified to show the resonance peak, with the initial peak in red, and the illuminated peak in black. From Figure 21, it is clear that the resonance frequency has decreased over the illumination time, and the peak also begins to broaden out at the edges, indicating a decrease in the quality factor as well; the amplitude of the peak also decreases, another sign of the lower Q factor. The main plot of Figure 20 shows this change in the resonance frequency and quality factor as a function of time, with intervals being measured every 10 seconds.

Using a simulated made by the Daneshmand group using HFSS and Advance Design System, the microwave circuit was simulated and materials with a variable complex permittivity were able to be put into the coupling gap. Using this method, the complex permittivity (a sum of the dielectric constant and an imaginary conductance term) of the TNTAMs could be found by matching the simulation to our measured results. The complex permittivity of the TNTAM before and after illumination by the 365 nm lamp was is shown in Table 3.2.

Table 3.2: Extracted Permittivities of TNTAM's

-	Before Illumination	After Illumination
Complex Permittivity ($\varepsilon_r = \varepsilon_r' + j\,\varepsilon_r''$)	$\varepsilon_r = 11 + j\,(0.11)$	$\varepsilon_r = 11.4 + j\,(0.15)$

As expected, the dielectric term increased after illumination due to charge carriers being excited and then trapped in the material. The bound charges left trapped in defect states within the bandgap are still more polarizable than if they were in the valence band. The conductance term also increased, indicating that some of those charge carriers remained untrapped in the material and added to the small current of the microwave circuit. These two phenomena have opposite effects on the resonant frequency (the former decreases it, the latter increases it) but the dominant effect is in the dielectric term and so we see a net decrease in f_0. Similarly, the Q factor is increased by the increasing dielectric constant, but the increase in current leads to more losses in the circuit, and there is a net overall decrease in Q. These trends are consistent regardless of the light source we use, so long as the light is absorbed and able to excite charge carriers in the material.

Other useful material parameters can be gained from the excitation and decay curves in Figure 20. Just like our TOF measurements, we can measure the recombination lifetimes of charge carriers after the light source has been turned off. Because the time scales are on the order of minutes to hours, high speed detection equipment is not needed beyond the speeds of the VNA. It is unlikely that there are any fast decay responses or excitation responses because those would likely show up as large instantaneous shifts in f_o or Q between two time intervals but none of those are present. Plots of the excitation and decay curves for the 254 nm and 405 nm experiment are shown in Figure 22 and 23.

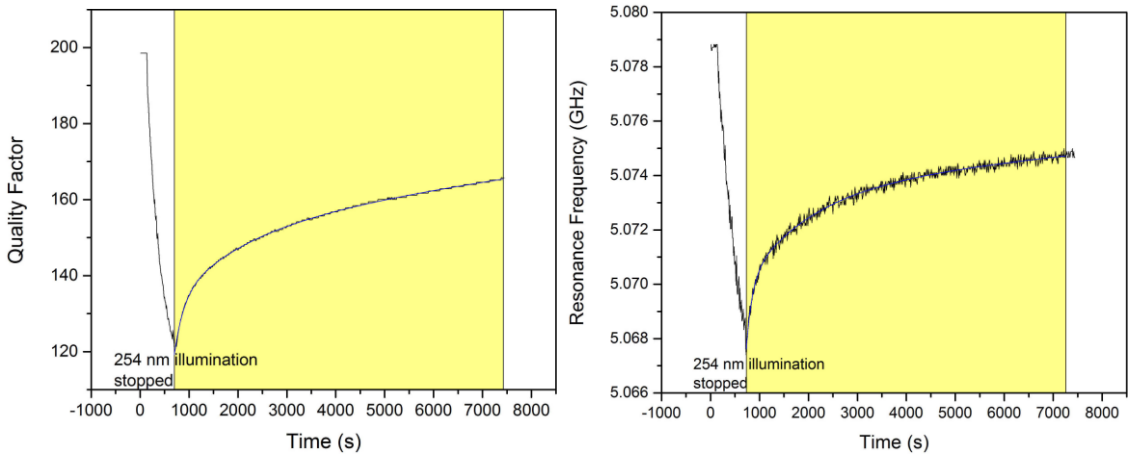

Figure 22: 254 nm illumination curves

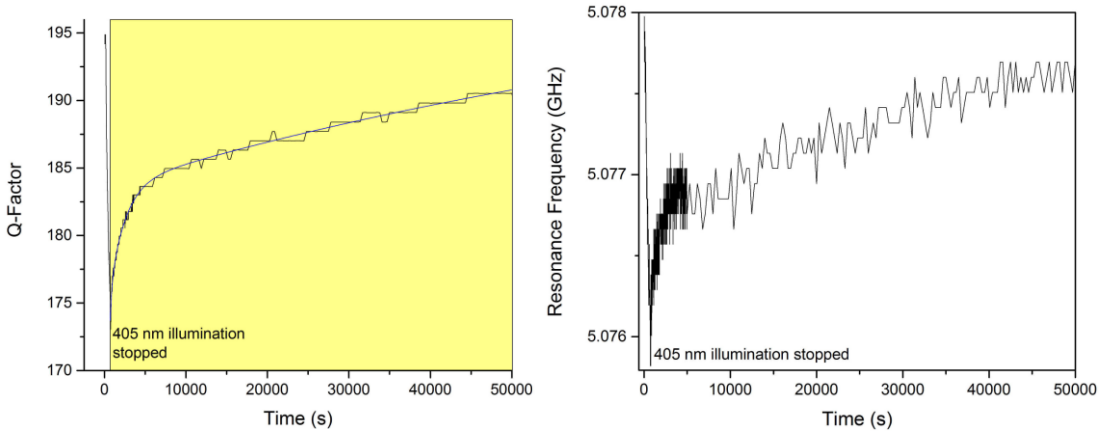

Figure 23: 405 nm illumination curves

The curves were best-fit to a triexponential response, indicating there are three recombination process occurring in the TNTAM; each with a different rate constant. These rate constants are also given component weights, representing how dominant a recombination process is within the TNTAM. The resonance frequency plots are much noisier than the Q-factor plots, likely because the change in signal is relatively much smaller than the signal value (only about 0.2%). A high signal to noise ratio in the f_o plots for the 365 nm and 405 nm make rate constant calculations less accurate. The rate constants and component weights for each of the processes are shown below in Table 3.3.

Table 3.3: Recombination lifetimes of TNTAM's with different Laser Sources

-	Recombination Lifetimes and Component Weights		
Laser Source and Resonance Parameter	τ_1 (s)	τ_2 (s)	τ_3 (s)
254 nm, Q	185.9 (5.2%)	1403.8 (19.6%)	21288.1 (75.2%)
254 nm, f_o	119.3 (8.5%)	1315.3 (24.3%)	39499.6 (67.2%)
365 nm, Q	213.3 (0.45%)	1410.2 (9.0%)	76589.5 (90.5%)
405nm, Q	181.8 (6.8%)	1852.5 (28.2%)	92951.2 (65.0%)

Though the time constants and component weights do not match identically between the laser sources, there is a lot of explanation for error because the TNTAMs are difficult to measure to the exact same size, identical placement within the coupling gap is also very subject to human error, and TNTAM fabrication and annealing is somewhat variable. Fortunately, there are three distinct rate constants for recombination, which can be broken up into 2-4 minutes (short), 20-30 minutes (medium) and 6-20 hours (long). Identifying these rate constants into physical phenomena is possible. The long lifetime is the slowest and most heavily weighted process, indicating it is likely caused by deep surface traps; it is also slightly more dominant in the 365 nm and 254 nm experiments, where the low penetration depths would only excite charge carriers very close to the surface. The medium

and short lifetime is thought to be electrons and holes being trapped in shallower traps of two distinct energies, resulting in two different rates.

3.2.3 Discussion

Time resolved microwave conductivity is a useful and relatively newer method for characterizing material parameters in the low frequency microwave regime. This was a fruitful partnership with the Daneshmand group because it gave us a use for the delaminated TiO_2 membranes and the complex permittivity ended up having strong response to the UV light, showing the unique abilities of the microwave resonators. The methods developed for these TRMC experiments are much easier to set up, manipulate the sample, and record data than previous experiments using a cavity waveguide resonator, which is bulky and hard to use.

TiO_2 membranes were characterized using the TRMC method and we found that the complex permittivity could be accurately found using the ADS simulations matched with our experiments. The transient data was used to measure the long-lived charge recombination lifetimes in the TNTAMs, and evidence suggests that the triexponential lifetime is evidence of deep surface traps (common on TiO_2 nanostructures), as well as more shallow traps with faster recombination.

There is also a lot of room for the planar microwave resonators to grow. As an example, the quality factor has been increased in newer resonators; and the sharper peaks make minor

changes to the sample result in huge measurable changes in resonance frequency and Q factor. Another improvement made to the resonator is to introduce a second identical resonator to measure variation in the local environment. That way only variation between the first and second resonators can be considered to be from changes to the material. This is important because as the sensitivity of the microwave resonator improves, it will be necessary to filter out environmental effects.

One of the most prominent directions of growth for this practice is in use as a sensing device. Since the resonator response changes strongly as material properties change, a well-calibrated microwave circuit could show when light is illuminated on a light-sensitive sample, or when oxygen is present near an oxygen-sensitive material. Current work is being done on using a high Q-factor resonator circuit as an ultra-sensitive light detector.

3.3 Measuring Phosphorescence of Tellurophenes

Tellurophenes are compounds of great interest for OLED devices. It is known that the heavy tellurium atom can induce spin-orbit coupling, and lead to singlet-to-triplet state transitions of the electron. Understanding and improving upon this process could lead to efficient phosphorescence in solid-state materials, something that is currently lacking in the literature.

The Rivard group in the Chemistry Department at the University of Alberta developed a new synthesis for colour-tunable tellurophenes. The goal of this research was to study the photoluminescence properties of those tellurophenes. This included measuring not only their photoluminescence (PL) spectrum, but also the quantum yield of each compound, the time-resolved photoluminescence of each compound, and whether the emission was affected by a highly oxygenated environment – something that can often cause quenching of the PL.

3.3.1 Experimental Setup

The compounds were given to us in powder form, and each was a tellurophene compound with different side groups, either a phenyl or pinacolboronate (BPin) group filling three different spots along the tellurophene ring. For use in devices, the compounds would need to be made into solid films from their powdered forms. We dissolved the compounds in Tetrahydrofuran (THF) at a concentration of 40 $mg\ mL^{-1}$. Glass slides were cleaned with acetone, methanol, and water under ultrasonication, then dried with nitrogen. The compounds were drop coated onto the cleaned glass slides using 200 μL of solution, and allowed to sit in a nitrogen-rich environment for 3 hours until they crystallized.

3.3.2 Photoluminescence of Tellurophenes

The solid tellurophene films were free of pinholes and uniform in shape and color. Photoluminescence spectra was measured using a Cary Eclipse spectrofluorometer using an excitation wavelength of 337 nm, and a detector gain of 600 V. The PL spectrum of

each compound is shown below in Figure 24 and 25, with an inset of their chemical structure.

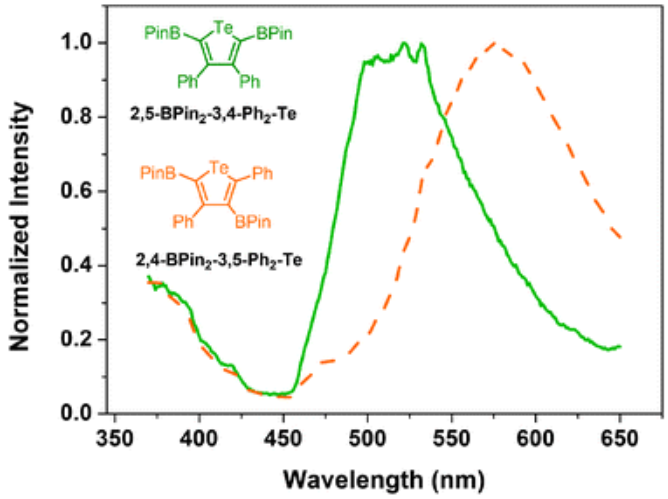

Figure 24: The two most photoluminescent compounds of the batch, Ph2-Green and Ph2-yellow [102]

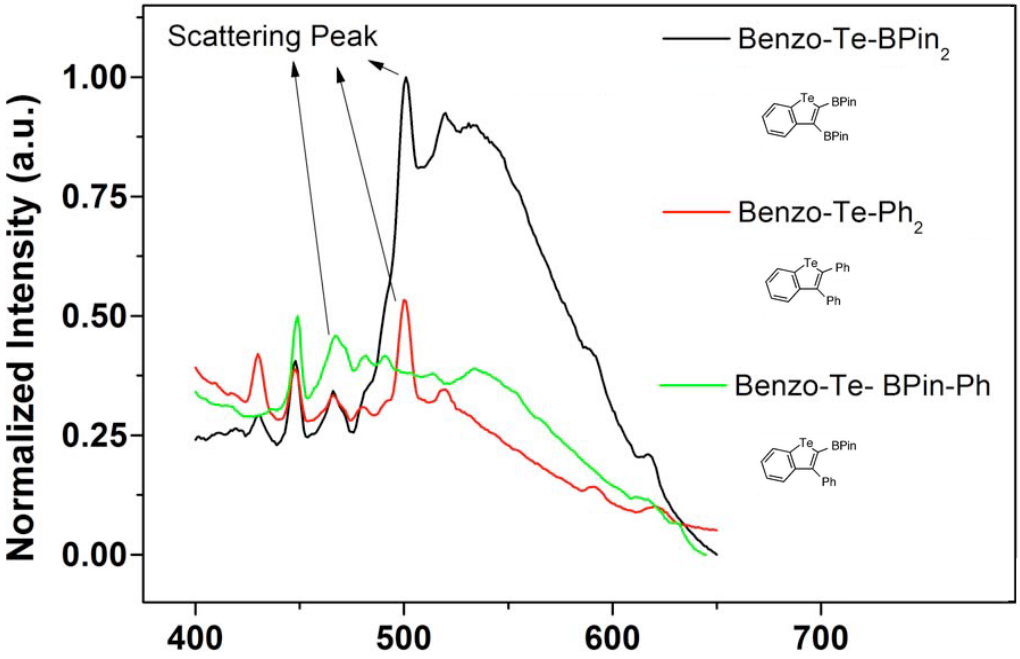

Figure 25: The remaining three compounds made by the Rivard group, they are all showing emission around 530 nm, but much less than the other two compounds. Adapted from [102]

The tellurophene samples show emission between 500 and 600 nm. This is a wide range of colour-tunability compared to previous reports in the literature. The two most photoluminescent films were the 2,5-$BPin_2$-3,5-Ph_2-Te (Ph2-Green) and 2,4-$BPin_2$-3,5-Ph_2-Te (Ph2-Yellow). The Benzo-Te-BPin-Ph molecule was strongly photoluminescent in THF:water (5:95) solution, but much less so in solid state; this indicates aggregation induced quenching occurs in some of the materials but not others. Alternatively, the Benzo-Te-$BPin_2$ was weakly emissive in solution, but showed a strong photoluminescence signal in the solid state, indicating crystallization-induced emission. The Benzo-Te-Ph_2 was weakly emissive in both solid state and solution, which means that a BPin group is likely necessary for strong photoluminescence, the necessity of the BPin group is something that has been seen previously in the literature.

After fabrication of the tellurophene samples, we did not keep them in a nitrogen rich environment for our initial tests. Therefore the compounds are shown to maintain photoluminescence over a period of a few days. A high intensity light test was done later and it showed that the organic Ph2-Green is stable even under direct illumination by a 180W sodium lamp, whereas less stable thiophenes lost their emission after about 5 minutes of exposure and this result is shown in Figure 26.

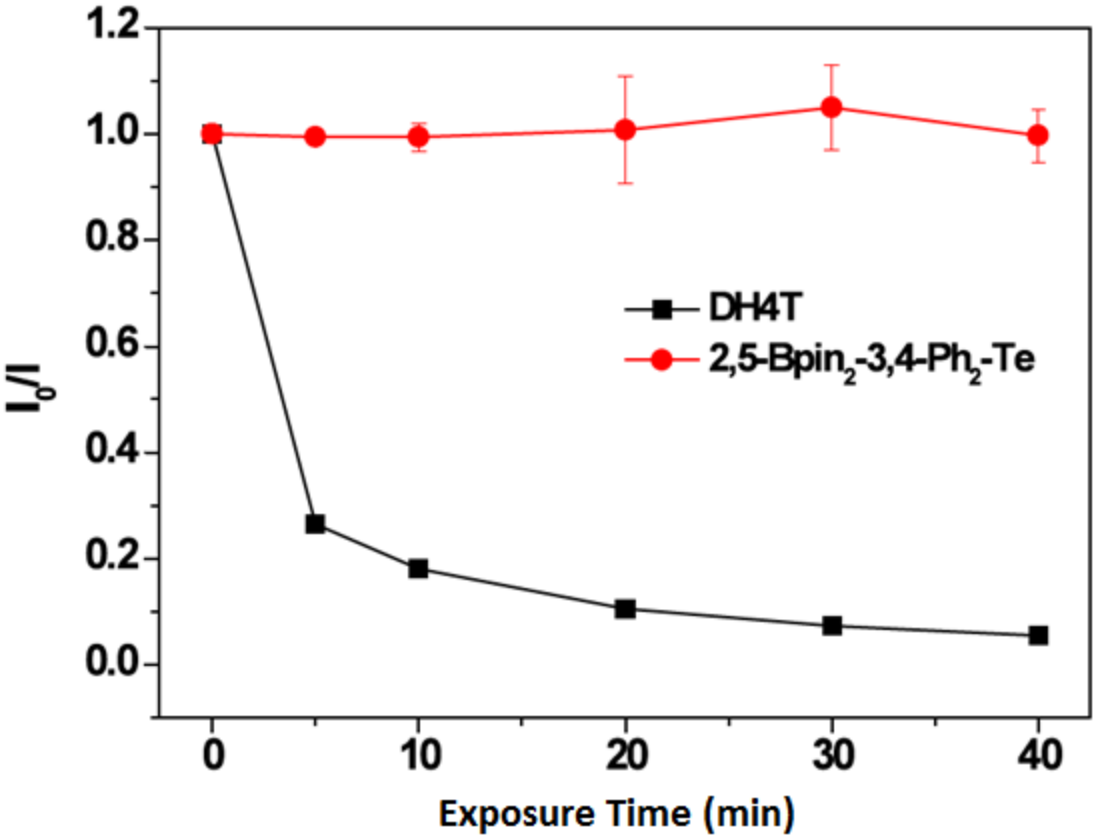

Figure 26: Ph2-Green maintains its original emission after exposure to high heat and light intensity, Dihexylquaterthiophene, a known photoluminescent material breaks down[102]

Quantifying the photoluminescence requires additional scans and a different scanning procedure that will ensure all of the emitted light is accounted for. We use the method designed by Friend *et al.* [119]which uses an integrating sphere to prevent any light being lost to the environment once it has entered the system. The quantum yield represents the ratio of light emitted to light absorbed by a material, so we run a series of measurements described in section 2.3.5 and use the data with equation 10. The results of the quantum yield measurements are shown below in Table 3.4.

Table 3.4: Photoluminescence and Quantum Yield of Tellurophenes

Compound	Peak Emission Wavelength	Quantum Yield
Ph2-Green	517 nm	4.5%
Ph2-Yellow	577 nm	5.3%
Benzo-Te-$BPin_2$	532 nm	1.3%
Benzo-Te-Ph_2	-	-
Benzo-Te-BPin-Ph	535 nm	Too low to measure

Further quantification was done by measuring the time-resolved photoluminescence, this was done with a pulsed laser source and a fast photomultiplier tube. The 337 nm laser pulse excites charge carriers in the tellurophene, and these decay to emit light, which is directed and filtered to the photomultiplier tube (PMT) and recorded as a voltage signal on an oscilloscope. The TRPL results for all compounds are found by fitting the emission decay to a single exponential function, and calculating the time constant. The results are shown below in Table 3.5, the PMT gain was high enough that even the weakest luminescent material, Benzo-Te-Ph_2, had a distinguishable signal.

Table 3.5: Photoluminescence Lifetime of Tellurophenes

Compound	Photoluminescence Lifetime (μs)
Ph2-Green	51.7
Ph2-Yellow	17.9
Benzo-Te-$BPin_2$	6.1
Benzo-Te-Ph_2	9.6
Benzo-Te-BPin-Ph	59.3

These lifetimes are all in the nanosecond range, indicating that each compound studied exhibits primarily phosphorescence. A fast emission was also detected for these compounds but it did not align with the expected PL spectrum and was most likely electronic noise from the laser pulse being picked up by the PMT, or it could have been the laser pulse being incompletely filtered by the monochromator. The lifetime data correlates well with the quantum yield data, and the phosphorescence of the samples can explain why the quantum yield may be difficult to increase. As expected, phosphorescent materials have a low quantum yield because their long lifetime makes carriers susceptible to quenching or non-radiative recombination over longer time periods.

Interestingly, the effect of oxygen quenching with these compounds was found to be already quite limited. Oxygen quenching is often a major source of loss in phosphorescent materials so it was investigated as a source of loss in our materials. This was done by testing 3 different environments for the tellurophenes. First, the Ph2-Green film was made

in a nitrogen glovebox (O_2 < 50ppm) and transferred to the spectrofluorometer in a nitrogen sealed container. Second, the Ph2-Green film was made at normal oxygen conditions, then put in a high pressure reaction chamber with 400 kPa (~4 atm) of pure oxygen. The third test was a Ph2-Green film made under normal conditions. The results are shown in Figure 27.

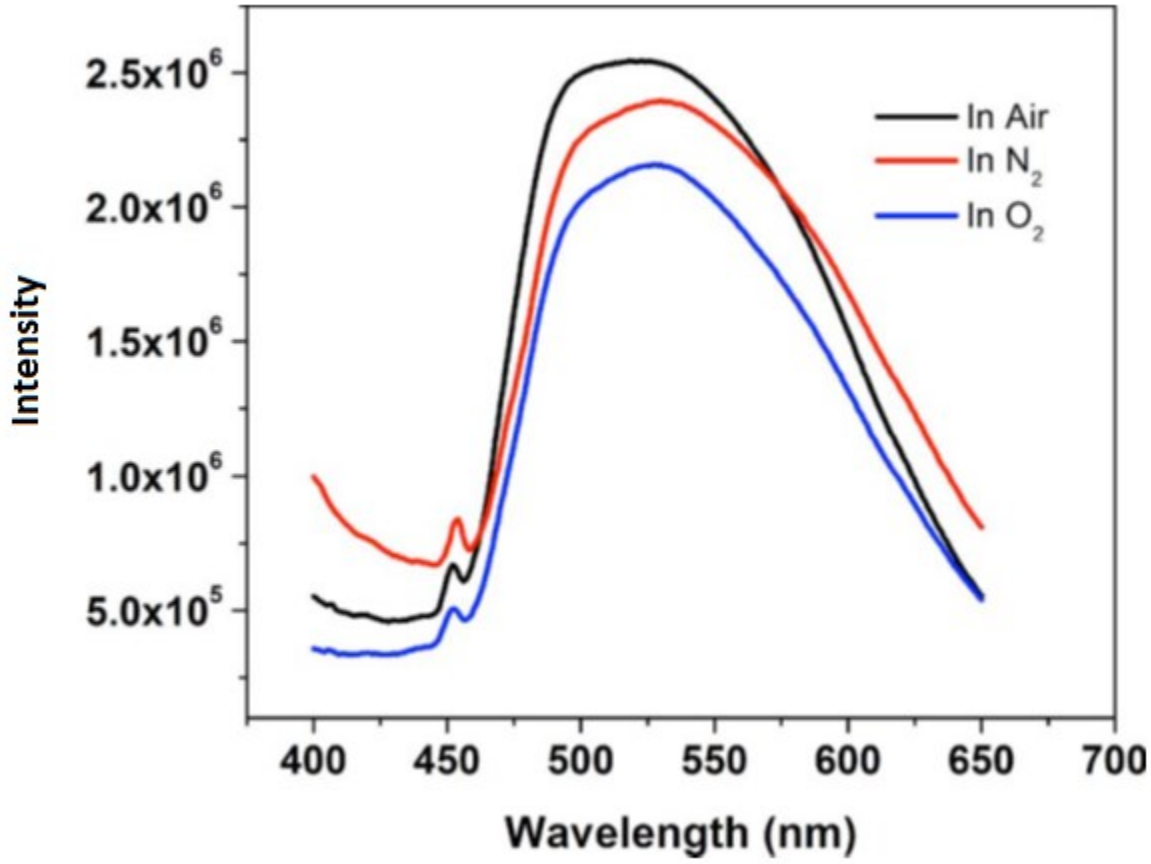

Figure 27: PL of Ph2-Green in varying oxygen environments [102]

The data shows no discernible trend between the presence of oxygen and decreased phosphorescence, indicating that oxygen quenching does not greatly affect the phosphorescence which is beneficial but uncommon in most organic emitters.

3.3.3 Discussion

The photoluminescence of the tellurophenes provided by the Rivard group was unique for many reasons. First, the photoluminescence was tunable by changing the functional groups on the tellurophene ring; and this was accomplished with only minor changes in chemical synthesis. Second, using the methods developed by Friend et al. we found the quantum yield to be quite low. This was later found to be a likely consequence of the phosphorescent nature of the tellurophene emission, which we found from an analysis of the emission lifetimes.

The phosphorescence was also unaffected by oxygen in the environment, indicating that oxygen quenching is not a pathway of loss for the Ph2-Green tellurophene. This will likely make the tellurophenes a key area of interest for OLED or biological marking applications. While improvements made to the tellurophene compounds are out of my expertise it is likely that even the materials presented above, specifically the Ph2-Green and Ph2-Yellow, could be useful in light emitting devices or applications as they are shown.

3.4 Charge Carrier Dynamics of Tellurophenes

Due to the unique photoluminescence properties of the tellurophenes, it makes sense to further characterize their material properties for potential device applications. In this section, the charge carrier dynamics of tellurophenes provided by the Rivard group are

studied. With adequate charge transport, the environmental stability of tellurophenes combined with their colour tenability could make them very useful as OLEDs.

3.4.1 Experimental Setup

The tellurophene provided by Dr. Rivard was known as B-6-Te-B, it is a tellurophene compound with two BPin side groups. We made multiple films by dissolving 40 $mgmL^{-1}$ of the compound in THF and drop-coating it onto cleaned FTO or spin coating it onto cleaned FTO at 2000 rpm. The powder was also thermally evaporated into a film using a PVD-75 organics evaporator. The chemical structure and optical properties of the three films are shown in Figure 28.

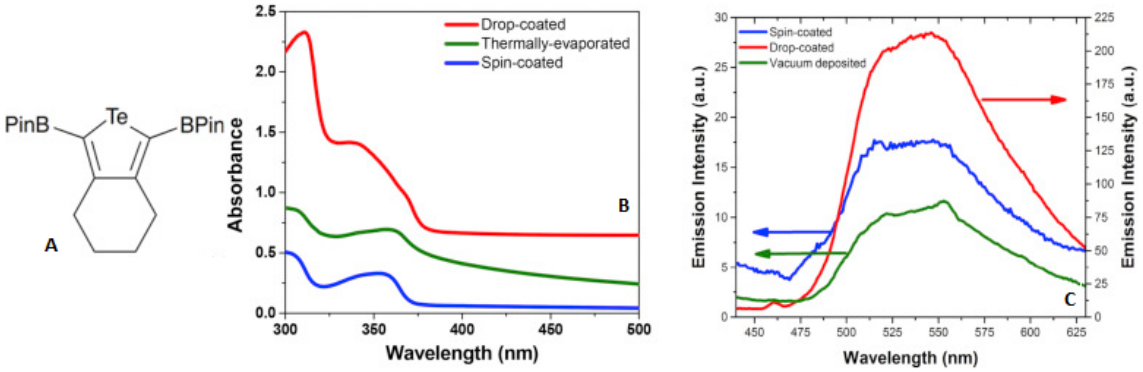

Figure 28: The chemical structure of B-6-Te-B (A) and its absorbance (B) and photoluminescence (C) in solid state. [101]

The photoluminescence spectra and the UV-Vis absorption spectra show that the drop-coated film has the highest PL peak at 500-550 nm and the highest absorbance. This indicates that the drop-coated film is the most crystalline. The absorbance plot shows that

the drop-coated film will absorb below ~375 nm, and the excitation wavelength for PL was set to be 350 nm. Below 320 nm the light is absorbed by the FTO and using an excitation signal below this value could skew the PL results.

3.4.2 Photoluminescence and Charge Transport Results

By using the same methods from section 3.3.2, we collected a quantum yield and emission lifetime for the drop-coated tellurophene samples. The quantum yield was found to be 11.5% and the emission lifetime was measured at 18 μs. This puts the B-6-Te-B tellurophene well within the class of phosphorescent tellurophenes; and it has a relatively high quantum yield. The tellurophene compound is also very stable in ambient atmosphere; and it maintained its photoluminescence even after years of initial fabrication, something that is very uncommon in organic phosphorescent materials.

An experiment called Time-Resolved Dark Injection (TRDI) was done to quantify the charge transport capabilities of the B-6-Te-B compound. This uses the pulse mode on the Keithley Semiconductor Parameter Analyzer by creating a large current pulse at one side of the sample at a specified time and measuring the collection of the current on the other side[125]. Dark injection is similar to time of flight in that it is a method to find the mobility of the charge carriers, and each respective method has its own advantages and disadvantages. TOF was done on these samples but the signal was too broad and a transit time could not be calculated. The light was either not absorbed in a small enough penetration depth, the dielectric relaxation time of the material was too fast, or re-emission

of the light was absorbed by defects or dopants and caused significant signal dispersion. The former is the most likely problem, as the dielectric relaxation time of these organics is expected to be slow because of their mediocre conductivity; and re-emission of light causing signal dispersion would likely show up in the dark injection measurements, which was not the case. Dark injection was able to measure the transit time in this case because it does not rely on material absorption but rather a voltage pulse to inject excess carriers into the material. Because of the similarity of the two methods; equation 4 still applies and was used to calculate a hole mobility of $1.1 \times 10^{-4} cm^2 V^{-1} s^{-1}$. The electron mobility was difficult to calculate because the Keithley pulse mode was not able to measure a long enough time interval, that can at least be used to estimate the electron mobility as being less than $10^{-6} cm^2 V^{-1} s^{-1}$. The hole mobility of the drop coated film is orders of magnitude higher than for the spin-coated or thermally evaporated film, indicating the film crystallinity has a large effect on the charge transport.

3.4.3 Discussion

We completed a series of experiments to see the potential of the B-6-Te-B tellurophene compounds for use in electronic devices. The B-6-Te-B was similar to the other tellurophenes of section 3.3 in that it had a long emission lifetime, a relatively high quantum yield, and exceptional stability. The hole mobility was adequate in the drop-coated film, and it would be ideal to make prototype OLEDs using these methods. It would also be interesting to use cathodoluminescence tests on all of these materials, in order to see the effectiveness of injected electrons in creating light emission.

Due to limitations in material preparation, all of the tellurophenes could not be characterized, especially since we needed about 10 mg of the powder for each film we made. Other potential candidates for OLEDs would be the Ph2-Green and Ph2-Yellow compounds but we were not able to test their charge transport, though we already know they have excellent PL properties and stability.

Chapter 4: Conclusion and Future Research Directions

This work focused on measuring carrier dynamics (inclusive of photoluminescence) in two different semiconducting material systems, namely TiO_2 nanostructures and organic tellurophenes. Optoelectronic characterization of these material systems is important, especially for use in electronic devices, and it is necessary to know the material properties in order to use them most effectively for applications.

Anatase-phase TiO_2 nanoparticles and polycrystalline thin films are popular electron transport layers in devices such as perovskite solar cells and OLEDs, and are also commonly used in gas and UV sensing. It remains to be seen if TiO_2 nanotubes and nanowires become as technologically significant as other forms of TiO_2. As a transport layer, TiO_2 nanowires were shown to have very low mobility compared to bulk TiO_2 due to a high density of deep traps on the surface of the nanowires. The TOF and IV analysis involved in this discovery are not commonly used, but they can prove very useful for understanding differences between nanostructures and bulk materials, especially when it comes to traps. We were able to passivate the deep traps using an ODPA SAM and improve the carrier mobility by a factor of almost 1000.

10-100μm thick free-standing TiO_2 nanotube membranes are of great interest for macromolecule filtration, drug delivery, substrates for cell cultures and substrate-assisted laser induced desorption mass spectrometry (SALDI) but it was not until their use in microwave sensing that they had a niche optoelectronic application. The goal of the TRMC

work was to characterize the transient complex permittivity of TiO_2 nanotubes during exposure to UV light and shed light on the underlying carrier dynamics. While there had been several papers to measure the microwave conductivity in TiO_2 thin films and nanoparticles using conventional cavity waveguide resonators, there were almost no reports that used planar microwave resonators. Planar microwave resonators are not merely compact, inexpensive and easier to fabricate, but also offer profound advantages in terms of the orders of magnitude higher Q-factors possible, the ability to easily monitor both the real and imaginary parts of the complex permittivity, the ability to apply both DC bias and illumination at the same time, and also the opportunity to introduce custom ambients during the measurement of the microwave response. In the process of performing the microwave characterization of titania nanotube membranes, it was found that the principles of TRMC could easily be applied to sensing applications, and the TiO_2-UV light dynamic was just one of many material-environment interactions that could be tracked using this method. Future work in this project can proceed in either one of two major directions; a more comprehensive characterization of material permittivity in the microwave to terahertz frequency regime, or improving the experimental methods so the system can function as an accurate and selective sensor for analytes such as light, small molecules, metal ions, and biomolecules. There is significant work that can be done in this field on both the material side and the sensing side.

The organic tellurophenes were studied because they had new and interesting color tunability in an organic tellurophene molecule, something which is often non-radiative. In order to further explore the results, it was necessary to setup quantitative tests that could

accurately describe this new photoluminescence such as quantum yield and time resolved photoluminescence. This proved to be effective because each test gave us more insight into the nature of the compounds. The materials were all phosphorescent with a lifetime in the range of 10 μs, the more strongly emitting ones having a relatively high quantum yield around 5%. The BPin group that had been previously suggested as being necessary for emission was again shown to be necessary. There was also evidence of crystallization induced phosphorescence in the Benzo-Te-$BPin_2$, which is in line with when we found that high crystallinity is a huge factor in emission intensity for the B-6-Te-B compound in section 3.4. The compounds also showed no signs of degradation over time, or when exposed to high light intensity, or when kept in a high oxygen environment; all things that are common issues for organic light emitters. The tellurophenes showed such interesting PL properties that their charge transport was measured with the goal being to really see the potential of these materials in OLEDs. The hole mobility measurement of $1.1 \times 10^{-4} cm^2 V^{-1} s^{-1}$ indicates it could be possible, but a prototype has not yet been made. Further study is probably necessary before their use in devices, but these materials are so luminescent and stable that their use in devices should continue to be investigated.

References

[1] R. P. Feynman, "There's plenty of room at the bottom," *Engineering and science,* vol. 23, pp. 22-36, 1960.

[2] T. V. Duncan, "Applications of nanotechnology in food packaging and food safety: barrier materials, antimicrobials and sensors," *Journal of colloid and interface science,* vol. 363, pp. 1-24, 2011.

[3] R. K. Sastry, S. Anshul, and N. Rao, "Nanotechnology in food processing sector-An assessment of emerging trends," *Journal of food science and technology,* vol. 50, pp. 831-841, 2013.

[4] X. He and H.-M. Hwang, "Nanotechnology in food science: Functionality, applicability, and safety assessment," *journal of food and drug analysis,* vol. 24, pp. 671-681, 2016.

[5] Y. Liu, X. Chen, and J. Xin, "Super-hydrophobic surfaces from a simple coating method: a bionic nanoengineering approach," *Nanotechnology,* vol. 17, p. 3259, 2006.

[6] S.-M. Lee and T. H. Kwon, "Mass-producible replication of highly hydrophobic surfaces from plant leaves," *Nanotechnology,* vol. 17, p. 3189, 2006.

[7] J. Pan, X. Song, J. Zhang, H. Shen, and Q. Xiong, "Switchable wettability in SnO2 nanowires and SnO2@ SnO2 heterostructures," *The Journal of Physical Chemistry C,* vol. 115, pp. 22225-22231, 2011.

[8] G. Thilagavathi, A. Raja, and T. Kannaian, "Nanotechnology and protective clothing for defence personnel," *Defence Science Journal,* vol. 58, p. 451, 2008.

[9] L. Lo, Y. Li, K. Yeung, and C. Yuen, "Indicating the development stage of nanotechnology in the textile and clothing industry," *International Journal of Nanotechnology,* vol. 4, pp. 667-679, 2007.

[10] K. Arivalagan, S. Ravichandran, K. Rangasamy, and E. Karthikeyan, "Nanomaterials and its potential applications," *International journal of chemtech research,* vol. 3, pp. 534-538, 2011.

[11] G. Shen, P.-C. Chen, K. Ryu, and C. Zhou, "Devices and chemical sensing applications of metal oxide nanowires," *Journal of Materials Chemistry,* vol. 19, pp. 828-839, 2009.

[12] Y. Li, F. Della Valle, M. Simonnet, I. Yamada, and J.-J. Delaunay, "High-performance UV detector made of ultra-long ZnO bridging nanowires," *Nanotechnology,* vol. 20, p. 045501, 2008.

[13] M.-W. Ahn, K.-S. Park, J.-H. Heo, J.-G. Park, D.-W. Kim, K. J. Choi*, et al.*, "Gas sensing properties of defect-controlled ZnO-nanowire gas sensor," *Applied physics letters,* vol. 93, p. 263103, 2008.

[14] J. Wilkinson, "Nanotechnology applications in medicine," *Medical device technology,* vol. 14, pp. 29-31, 2003.

[15] G. Balasundaram and T. J. Webster, "Nanotechnology and biomaterials for orthopedic medical applications," 2006.

[16] S. Prabhu and E. K. Poulose, "Silver nanoparticles: mechanism of antimicrobial action, synthesis, medical applications, and toxicity effects," *International Nano Letters,* vol. 2, p. 32, 2012.

[17] W.-N. Wang, W.-J. An, B. Ramalingam, S. Mukherjee, D. M. Niedzwiedzki, S. Gangopadhyay*, et al.*, "Size and structure matter: enhanced CO2 photoreduction

efficiency by size-resolved ultrafine Pt nanoparticles on TiO2 single crystals," *Journal of the American Chemical Society,* vol. 134, pp. 11276-11281, 2012.
[18] M. Paulose, O. K. Varghese, G. K. Mor, C. A. Grimes, and K. G. Ong, "Unprecedented ultra-high hydrogen gas sensitivity in undoped titania nanotubes," *Nanotechnology,* vol. 17, p. 398, 2005.
[19] F. Dong, W. Zhao, and Z. Wu, "Characterization and photocatalytic activities of C, N and S co-doped TiO2 with 1D nanostructure prepared by the nano-confinement effect," *Nanotechnology,* vol. 19, p. 365607, 2008.
[20] Y.-M. Chien, F. Lefevre, I. Shih, and R. Izquierdo, "A solution processed top emission OLED with transparent carbon nanotube electrodes," *Nanotechnology,* vol. 21, p. 134020, 2010.
[21] S. Jha, J.-C. Qian, O. Kutsay, J. Kovac Jr, C.-Y. Luan, J. A. Zapien*, et al.*, "Violet-blue LEDs based on p-GaN/n-ZnO nanorods and their stability," *Nanotechnology,* vol. 22, p. 245202, 2011.
[22] T.-H. Han, Y. Lee, M.-R. Choi, S.-H. Woo, S.-H. Bae, B. H. Hong*, et al.*, "Extremely efficient flexible organic light-emitting diodes with modified graphene anode," *Nature Photonics,* vol. 6, pp. 105-110, 2012.
[23] T. Stelzner, M. Pietsch, G. Andrä, F. Falk, E. Ose, and S. Christiansen, "Silicon nanowire-based solar cells," *Nanotechnology,* vol. 19, p. 295203, 2008.
[24] K. Shankar, G. K. Mor, H. E. Prakasam, S. Yoriya, M. Paulose, O. K. Varghese*, et al.*, "Highly-ordered TiO2 nanotube arrays up to 220 μm in length: use in water photoelectrolysis and dye-sensitized solar cells," *Nanotechnology,* vol. 18, p. 065707, 2007.
[25] H.-S. Kim, J.-W. Lee, N. Yantara, P. P. Boix, S. A. Kulkarni, S. Mhaisalkar*, et al.*, "High efficiency solid-state sensitized solar cell-based on submicrometer rutile TiO2 nanorod and CH3NH3PbI3 perovskite sensitizer," *Nano letters,* vol. 13, pp. 2412-2417, 2013.
[26] X. Rocquefelte, F. Goubin, H.-J. Koo, M.-H. Whangbo, and S. Jobic, "Investigation of the origin of the empirical relationship between refractive index and density on the basis of first principles calculations for the refractive indices of various TiO2 phases," *Inorganic chemistry,* vol. 43, pp. 2246-2251, 2004.
[27] D. O. Scanlon, C. W. Dunnill, J. Buckeridge, S. A. Shevlin, A. J. Logsdail, S. M. Woodley*, et al.*, "Band alignment of rutile and anatase TiO2," *Nature materials,* vol. 12, pp. 798-801, 2013.
[28] J. Zhang, P. Zhou, J. Liu, and J. Yu, "New understanding of the difference of photocatalytic activity among anatase, rutile and brookite TiO2," *Physical Chemistry Chemical Physics,* vol. 16, pp. 20382-20386, 2014.
[29] H. Park, Y. Park, W. Kim, and W. Choi, "Surface modification of TiO 2 photocatalyst for environmental applications," *Journal of Photochemistry and Photobiology C: Photochemistry Reviews,* vol. 15, pp. 1-20, 2013.
[30] Y. Xie, L. Wei, Q. Li, Y. Chen, S. Yan, J. Jiao*, et al.*, "High-performance self-powered UV photodetectors based on TiO2 nano-branched arrays," *Nanotechnology,* vol. 25, p. 075202, 2014.
[31] Y. Zhao and K. Zhu, "Charge transport and recombination in perovskite (CH3NH3) PbI3 sensitized TiO2 solar cells," *The Journal of Physical Chemistry Letters,* vol. 4, pp. 2880-2884, 2013.

[32] W.-Q. Wu, B.-X. Lei, H.-S. Rao, Y.-F. Xu, Y.-F. Wang, C.-Y. Su*, et al.*, "Hydrothermal fabrication of hierarchically anatase TiO2 nanowire arrays on FTO glass for dye-sensitized solar cells," *Scientific reports,* vol. 3, p. 1352, 2013.
[33] B. A. Al-Asbahi, M. H. Haji Jumali, and M. S. AlSalhi, "Enhanced Optoelectronic Properties of PFO/Fluorol 7GA Hybrid Light Emitting Diodes via Additions of TiO2 Nanoparticles," *Polymers,* vol. 8, p. 334, 2016.
[34] R. Fateh, R. Dillert, and D. Bahnemann, "Self-Cleaning properties, mechanical stability, and adhesion strength of transparent photocatalytic TiO2–ZnO coatings on polycarbonate," *ACS applied materials & interfaces,* vol. 6, pp. 2270-2278, 2014.
[35] C. Sotelo-Vazquez, N. Noor, A. Kafizas, R. Quesada-Cabrera, D. O. Scanlon, A. Taylor*, et al.*, "Multifunctional P-doped TiO2 films: a new approach to self-cleaning, transparent conducting oxide materials," *Chemistry of Materials,* vol. 27, pp. 3234-3242, 2015.
[36] A. M. Zaky and B. P. Chaplin, "Porous substoichiometric TiO2 anodes as reactive electrochemical membranes for water treatment," *Environmental science & technology,* vol. 47, pp. 6554-6563, 2013.
[37] G. Ghasemzadeh, M. Momenpour, F. Omidi, M. R. Hosseini, M. Ahani, and A. Barzegari, "Applications of nanomaterials in water treatment and environmental remediation," *Frontiers of Environmental Science & Engineering,* vol. 8, pp. 471-482, 2014.
[38] H. Xu, S. Ouyang, P. Li, T. Kako, and J. Ye, "High-active anatase TiO2 nanosheets exposed with 95%{100} facets toward efficient H2 evolution and CO2 photoreduction," *ACS applied materials & interfaces,* vol. 5, pp. 1348-1354, 2013.
[39] D. Reyes-Coronado, G. Rodríguez-Gattorno, M. Espinosa-Pesqueira, C. Cab, R. d. de Coss, and G. Oskam, "Phase-pure TiO2 nanoparticles: anatase, brookite and rutile," *Nanotechnology,* vol. 19, p. 145605, 2008.
[40] H. G. Yang and H. C. Zeng, "Preparation of hollow anatase TiO2 nanospheres via Ostwald ripening," *The Journal of Physical Chemistry B,* vol. 108, pp. 3492-3495, 2004.
[41] H. Li, Y. Zeng, T. Huang, L. Piao, Z. Yan, and M. Liu, "Hierarchical TiO2 nanospheres with dominant {001} facets: facile synthesis, growth mechanism, and photocatalytic activity," *Chemistry–A European Journal,* vol. 18, pp. 7525-7532, 2012.
[42] C. A. Grimes and G. K. Mor, *TiO2 nanotube arrays: synthesis, properties, and applications*: Springer Science & Business Media, 2009.
[43] P. Roy, S. Berger, and P. Schmuki, "TiO2 nanotubes: synthesis and applications," *Angewandte Chemie International Edition,* vol. 50, pp. 2904-2939, 2011.
[44] C. A. Grimes, "Synthesis and application of highly ordered arrays of TiO 2 nanotubes," *Journal of Materials Chemistry,* vol. 17, pp. 1451-1457, 2007.
[45] Z. Miao, D. Xu, J. Ouyang, G. Guo, X. Zhao, and Y. Tang, "Electrochemically induced sol− gel preparation of single-crystalline TiO2 nanowires," *Nano Letters,* vol. 2, pp. 717-720, 2002.
[46] Y. Zhang, G. Li, Y. Jin, Y. Zhang, J. Zhang, and L. Zhang, "Hydrothermal synthesis and photoluminescence of TiO 2 nanowires," *Chemical Physics Letters,* vol. 365, pp. 300-304, 2002.
[47] J.-N. Nian and H. Teng, "Hydrothermal synthesis of single-crystalline anatase TiO2 nanorods with nanotubes as the precursor," *The Journal of Physical Chemistry B,* vol. 110, pp. 4193-4198, 2006.

[48] B. Liu and E. S. Aydil, "Growth of oriented single-crystalline rutile TiO2 nanorods on transparent conducting substrates for dye-sensitized solar cells," *Journal of the American Chemical Society,* vol. 131, pp. 3985-3990, 2009.
[49] P. D. Cozzoli, A. Kornowski, and H. Weller, "Low-temperature synthesis of soluble and processable organic-capped anatase TiO2 nanorods," *Journal of the American Chemical Society,* vol. 125, pp. 14539-14548, 2003.
[50] C. Cao, C. Hu, X. Wang, S. Wang, Y. Tian, and H. Zhang, "UV sensor based on TiO 2 nanorod arrays on FTO thin film," *Sensors and Actuators B: Chemical,* vol. 156, pp. 114-119, 2011.
[51] J. Zhang, M. Li, Z. Feng, J. Chen, and C. Li, "UV Raman spectroscopic study on TiO2. I. Phase transformation at the surface and in the bulk," *The Journal of Physical Chemistry B,* vol. 110, pp. 927-935, 2006.
[52] R. D. Shannon, "Phase Transformation Studies in TiO2 Supporting Different Defect Mechanisms in Vacuum-Reduced and Hydrogen-Reduced Rutile," *Journal of Applied Physics,* vol. 35, pp. 3414-3416, 1964.
[53] M. Kong, Y. Li, X. Chen, T. Tian, P. Fang, F. Zheng*, et al.*, "Tuning the relative concentration ratio of bulk defects to surface defects in TiO2 nanocrystals leads to high photocatalytic efficiency," *Journal of the American Chemical Society,* vol. 133, pp. 16414-16417, 2011.
[54] E. Logothetis and R. E. Hetrick, "Oscillations in the electrical resistivity of TiO2 induced by solid/gas interactions," *Solid State Communications,* vol. 31, pp. 167-171, 1979.
[55] F. Cardon, "Polarization and space-charge-limited currents in rutile (TiO2)," *Physica,* vol. 27, pp. 841-849, 1961.
[56] E. Hendry, M. Koeberg, B. O'regan, and M. Bonn, "Local field effects on electron transport in nanostructured TiO2 revealed by terahertz spectroscopy," *Nano letters,* vol. 6, pp. 755-759, 2006.
[57] I. Abayev, A. Zaban, F. Fabregat-Santiago, and J. Bisquert, "Electronic conductivity in nanostructured TiO2 films permeated with electrolyte," *PHYSICA STATUS SOLIDI A APPLIED RESEARCH,* vol. 196, pp. R4-R6, 2003.
[58] M. Dolata, P. Kedzierzawski, and J. Augustynski, "Comparative impedance spectroscopy study of rutile and anatase TiO2 film electrodes," *Electrochimica Acta,* vol. 41, pp. 1287-1293, 1996.
[59] P. De Jongh and D. Vanmaekelbergh, "Investigation of the electronic transport properties of nanocrystalline particulate TiO2 electrodes by intensity-modulated photocurrent spectroscopy," *The Journal of Physical Chemistry B,* vol. 101, pp. 2716-2722, 1997.
[60] H. Tang, K. Prasad, R. Sanjines, P. Schmid, and F. Levy, "Electrical and optical properties of TiO2 anatase thin films," *Journal of Applied Physics,* vol. 75, pp. 2042-2047, 1994.
[61] J. Van de Lagemaat and A. Frank, "Nonthermalized electron transport in dye-sensitized nanocrystalline TiO2 films: transient photocurrent and random-walk modeling studies," *The Journal of Physical Chemistry B,* vol. 105, pp. 11194-11205, 2001.
[62] R. G. Breckenridge and W. R. Hosler, "Electrical properties of titanium dioxide semiconductors," *Physical Review,* vol. 91, p. 793, 1953.
[63] D. Pan, N. Zhao, Q. Wang, S. Jiang, X. Ji, and L. An, "Facile synthesis and characterization of luminescent TiO2 nanocrystals," *Advanced materials,* vol. 17, pp. 1991-1995, 2005.

[64] D. M. King, X. Du, A. S. Cavanagh, and A. W. Weimer, "Quantum confinement in amorphous TiO2 films studied via atomic layer deposition," *Nanotechnology,* vol. 19, p. 445401, 2008.
[65] E. Baldini, L. Chiodo, A. Dominguez, M. Palummo, S. Moser, M. Yazdi-Rizi*, et al.*, "Strongly bound excitons in anatase TiO2 single crystals and nanoparticles," *Nature Communications,* vol. 8, 2017.
[66] E.-Z. Tan, P.-G. Yin, T.-t. You, H. Wang, and L. Guo, "Three dimensional design of large-scale TiO2 nanorods scaffold decorated by silver nanoparticles as SERS sensor for ultrasensitive malachite green detection," *ACS applied materials & interfaces,* vol. 4, pp. 3432-3437, 2012.
[67] T.-S. Kang, A. P. Smith, B. E. Taylor, and M. F. Durstock, "Fabrication of highly-ordered TiO2 nanotube arrays and their use in dye-sensitized solar cells," *Nano letters,* vol. 9, pp. 601-606, 2009.
[68] I. Bannat, K. Wessels, T. Oekermann, J. Rathousky, D. Bahnemann, and M. Wark, "Improving the photocatalytic performance of mesoporous titania films by modification with gold nanostructures," *Chemistry of Materials,* vol. 21, pp. 1645-1653, 2009.
[69] S. Farsinezhad, H. Sharma, and K. Shankar, "Interfacial band alignment for photocatalytic charge separation in TiO 2 nanotube arrays coated with CuPt nanoparticles," *Physical Chemistry Chemical Physics,* vol. 17, pp. 29723-29733, 2015.
[70] D. R. Baker and P. V. Kamat, "Photosensitization of TiO2 nanostructures with CdS quantum dots: particulate versus tubular support architectures," *Advanced Functional Materials,* vol. 19, pp. 805-811, 2009.
[71] K. Zhu, N. R. Neale, A. Miedaner, and A. J. Frank, "Enhanced charge-collection efficiencies and light scattering in dye-sensitized solar cells using oriented TiO2 nanotubes arrays," *Nano letters,* vol. 7, pp. 69-74, 2007.
[72] J. Jiang, F. Gu, W. Shao, and C. Li, "Fabrication of spherical multi-hollow TiO2 nanostructures for photoanode film with enhanced light-scattering performance," *Industrial & Engineering Chemistry Research,* vol. 51, pp. 2838-2845, 2012.
[73] M. A. Lampert, "Simplified theory of space-charge-limited currents in an insulator with traps," *Physical Review,* vol. 103, p. 1648, 1956.
[74] A. Rose, "Space-charge-limited currents in solids," *Physical Review,* vol. 97, p. 1538, 1955.
[75] A. Many and G. Rakavy, "Theory of transient space-charge-limited currents in solids in the presence of trapping," *Physical Review,* vol. 126, p. 1980, 1962.
[76] Y. Zhu and L. Ang, "Analytical re-derivation of space charge limited current in solids using capacitor model," *Journal of Applied Physics,* vol. 110, p. 094514, 2011.
[77] J. C. Love, L. A. Estroff, J. K. Kriebel, R. G. Nuzzo, and G. M. Whitesides, "Self-assembled monolayers of thiolates on metals as a form of nanotechnology," *Chemical reviews,* vol. 105, pp. 1103-1170, 2005.
[78] S. Brandriss and S. Margel, "Synthesis and characterization of self-assembled hydrophobic monolayer coatings on silica colloids," *Langmuir,* vol. 9, pp. 1232-1240, 1993.
[79] S. Farsinezhad, P. R. Waghmare, B. D. Wiltshire, H. Sharma, S. Amiri, S. K. Mitra*, et al.*, "Amphiphobic surfaces from functionalized TiO 2 nanotube arrays," *Rsc Advances,* vol. 4, pp. 33587-33598, 2014.

[80] Y. Feng, W. K. Teo, K. S. Siow, Z. Gao, K. L. Tan, and A. K. Hsieh, "Corrosion protection of copper by a self-assembled monolayer of alkanethiol," *Journal of The Electrochemical Society,* vol. 144, pp. 55-64, 1997.
[81] F. P. Zamborini and R. M. Crooks, "Corrosion passivation of gold by n-alkanethiol self-assembled monolayers: effect of chain length and end group," *Langmuir,* vol. 14, pp. 3279-3286, 1998.
[82] T. Wink, S. Van Zuilen, A. Bult, and W. Van Bennekom, "Self-assembled monolayers for biosensors," *Analyst,* vol. 122, pp. 43R-50R, 1997.
[83] J. J. Gooding, F. Mearns, W. Yang, and J. Liu, "Self-assembled monolayers into the 21st century: recent advances and applications," *Electroanalysis,* vol. 15, pp. 81-96, 2003.
[84] M. D. Malinsky, K. L. Kelly, G. C. Schatz, and R. P. Van Duyne, "Chain length dependence and sensing capabilities of the localized surface plasmon resonance of silver nanoparticles chemically modified with alkanethiol self-assembled monolayers," *Journal of the American Chemical Society,* vol. 123, pp. 1471-1482, 2001.
[85] B. de Boer, A. Hadipour, M. M. Mandoc, T. van Woudenbergh, and P. W. Blom, "Tuning of Metal Work Functions with Self-Assembled Monolayers," *Advanced Materials,* vol. 17, pp. 621-625, 2005.
[86] I. Campbell, S. Rubin, T. Zawodzinski, J. Kress, R. Martin, D. Smith*, et al.*, "Controlling Schottky energy barriers in organic electronic devices using self-assembled monolayers," *Physical Review B,* vol. 54, p. R14321, 1996.
[87] G. P. Lopez, M. W. Albers, S. L. Schreiber, R. Carroll, E. Peralta, and G. M. Whitesides, "Convenient methods for patterning the adhesion of mammalian cells to surfaces using self-assembled monolayers of alkanethiolates on gold," *Journal of the American Chemical Society,* vol. 115, pp. 5877-5878, 1993.
[88] Y. Arima and H. Iwata, "Preferential adsorption of cell adhesive proteins from complex media on self-assembled monolayers and its effect on subsequent cell adhesion," *Acta biomaterialia,* vol. 26, pp. 72-81, 2015.
[89] E. Balaur, J. M. Macak, L. Taveira, and P. Schmuki, "Tailoring the wettability of TiO 2 nanotube layers," *Electrochemistry Communications,* vol. 7, pp. 1066-1070, 2005.
[90] A. Mohammadpour, B. Wiltshire, Y. Zhang, S. Farsinezhad, A. Askar, R. Kisslinger*, et al.*, "100-fold improvement in carrier drift mobilities in alkanephosphonate-passivated monocrystalline TiO2 nanowire arrays," *Nanotechnology,* vol. 28, p. 144001, 2017.
[91] N. M. Hemed, A. Convertino, and Y. Shacham-Diamand, "Investigation of functionalized silicon nanowires by self-assembled monolayer," *Applied Surface Science,* vol. 367, pp. 231-236, 2016.
[92] H. Hinterwirth, S. Kappel, T. Waitz, T. Prohaska, W. Lindner, and M. Lämmerhofer, "Quantifying thiol ligand density of self-assembled monolayers on gold nanoparticles by inductively coupled plasma–mass spectrometry," *ACS nano,* vol. 7, pp. 1129-1136, 2013.
[93] S. K. Hau, H.-L. Yip, H. Ma, and A. K.-Y. Jen, "High performance ambient processed inverted polymer solar cells through interfacial modification with a fullerene self-assembled monolayer," *Applied Physics Letters,* vol. 93, p. 441, 2008.
[94] A. B. Sieval, R. Linke, H. Zuilhof, and E. J. Sudhölter, "High-quality alkyl monolayers on silicon surfaces," *Advanced Materials,* vol. 12, pp. 1457-1460, 2000.
[95] H. Ma, O. Acton, D. O. Hutchins, N. Cernetic, and A. K.-Y. Jen, "Multifunctional phosphonic acid self-assembled monolayers on metal oxides as dielectrics, interface modification layers and semiconductors for low-voltage high-performance organic field-

effect transistors," *Physical Chemistry Chemical Physics,* vol. 14, pp. 14110-14126, 2012.
[96] M. Samanta, W. Tian, S. Datta, J. Henderson, and C. Kubiak, "Electronic conduction through organic molecules," *Physical Review B,* vol. 53, p. R7626, 1996.
[97] S. R. Forrest and M. E. Thompson, "Introduction: organic electronics and optoelectronics," *Chemical Reviews,* vol. 107, pp. 923-925, 2007.
[98] Y. Olivier, V. Lemaur, J.-L. Brédas, and J. Cornil, "Charge hopping in organic semiconductors: Influence of molecular parameters on macroscopic mobilities in model one-dimensional stacks," *The Journal of Physical Chemistry A,* vol. 110, pp. 6356-6364, 2006.
[99] M. Kasha, "Characterization of electronic transitions in complex molecules," *Discussions of the Faraday society,* vol. 9, pp. 14-19, 1950.
[100] D. J. Griffiths, *Introduction to quantum mechanics*: Cambridge University Press, 2016.
[101] G. He, W. Torres Delgado, D. J. Schatz, C. Merten, A. Mohammadpour, L. Mayr*, et al.*, "Coaxing Solid-State Phosphorescence from Tellurophenes," *Angewandte Chemie International Edition,* vol. 53, pp. 4587-4591, 2014.
[102] G. He, B. D. Wiltshire, P. Choi, A. Savin, S. Sun, A. Mohammadpour*, et al.*, "Phosphorescence within benzotellurophenes and color tunable tellurophenes under ambient conditions," *Chemical Communications,* vol. 51, pp. 5444-5447, 2015.
[103] E. Rivard, "Tellurophenes and Their Emergence as Building Blocks for Polymeric and Light-emitting Materials," *Chemistry Letters,* vol. 44, pp. 730-736, 2015.
[104] R. Gillanders, M. Tedford, P. Crilly, and R. Bailey, "Thin film dissolved oxygen sensor based on platinum octaethylporphyrin encapsulated in an elastic fluorinated polymer," *Analytica chimica acta,* vol. 502, pp. 1-6, 2004.
[105] S. Lamansky, P. Djurovich, D. Murphy, F. Abdel-Razzaq, H.-E. Lee, C. Adachi*, et al.*, "Highly phosphorescent bis-cyclometalated iridium complexes: synthesis, photophysical characterization, and use in organic light emitting diodes," *Journal of the American Chemical Society,* vol. 123, pp. 4304-4312, 2001.
[106] M. Zander and G. Kirsch, "On the phosphorescence of benzologues of furan, thiophene, selenophene, and tellurophene. A systematic study of the intra-annular internal heavy-atom effect," *Zeitschrift für Naturforschung A,* vol. 44, pp. 205-209, 1989.
[107] M. Paulose, K. Shankar, S. Yoriya, H. E. Prakasam, O. K. Varghese, G. K. Mor*, et al.*, "Anodic growth of highly ordered TiO2 nanotube arrays to 134 μm in length," *The Journal of Physical Chemistry B,* vol. 110, pp. 16179-16184, 2006.
[108] J. Wang and Z. Lin, "Freestanding TiO2 nanotube arrays with ultrahigh aspect ratio via electrochemical anodization," *Chemistry of Materials,* vol. 20, pp. 1257-1261, 2008.
[109] S. P. Albu, A. Ghicov, J. M. Macak, R. Hahn, and P. Schmuki, "Self-organized, free-standing TiO2 nanotube membrane for flow-through photocatalytic applications," *Nano letters,* vol. 7, pp. 1286-1289, 2007.
[110] X. Feng, K. Shankar, O. K. Varghese, M. Paulose, T. J. Latempa, and C. A. Grimes, "Vertically aligned single crystal TiO2 nanowire arrays grown directly on transparent conducting oxide coated glass: synthesis details and applications," *Nano letters,* vol. 8, pp. 3781-3786, 2008.
[111] Z. Wei, Y. Yao, T. Huang, and A. Yu, "Solvothermal growth of well-aligned TiO2 nanowire arrays for dye-sensitized solar cell: dependence of morphology and vertical

orientation upon substrate pretreatment," *Int. J. Electrochem. Sci,* vol. 6, pp. 1871-1879, 2011.
[112] A. Kumar, A. R. Madaria, and C. Zhou, "Growth of aligned single-crystalline rutile TiO2 nanowires on arbitrary substrates and their application in dye-sensitized solar cells," *The Journal of Physical Chemistry C,* vol. 114, pp. 7787-7792, 2010.
[113] Y. Li, L. Wei, X. Chen, R. Zhang, X. Sui, Y. Chen*, et al.*, "Efficient PbS/CdS co-sensitized solar cells based on TiO 2 nanorod arrays," *Nanoscale research letters,* vol. 8, p. 67, 2013.
[114] Y.-Y. Song, F. Schmidt-Stein, S. Bauer, and P. Schmuki, "Amphiphilic TiO2 nanotube arrays: an actively controllable drug delivery system," *Journal of the American Chemical Society,* vol. 131, pp. 4230-4232, 2009.
[115] A. Mohammadpour, S. Farsinezhad, B. D. Wiltshire, and K. Shankar, "Majority carrier transport in single crystal rutile nanowire arrays," *physica status solidi (RRL)-Rapid Research Letters,* vol. 8, pp. 512-516, 2014.
[116] J. Kočka, O. Klíma, G. Juška, M. Hoheisel, and R. Plättner, "SCLC transients in a-Si: H—new features and possibilities," *Journal of non-crystalline solids,* vol. 137, pp. 427-430, 1991.
[117] B. Olson, "Time-resolved measurements of charge carrier dynamics and optical nonlinearities in narrow-bandgap semiconductors," 2013.
[118] W. Domcke, "Analytic theory of resonances, virtual states and bound states ion electron-molecule scattering and related processes," *Journal of Physics B: Atomic and Molecular Physics,* vol. 14, p. 4889, 1981.
[119] N. Greenham, I. Samuel, G. Hayes, R. Phillips, Y. Kessener, S. Moratti*, et al.*, "Measurement of absolute photoluminescence quantum efficiencies in conjugated polymers," *Chemical physics letters,* vol. 241, pp. 89-96, 1995.
[120] L.-O. Pålsson and A. P. Monkman, "Measurements of solid-state photoluminescence quantum yields of films using a fluorimeter," *Advanced Materials,* vol. 14, p. 757, 2002.
[121] M. Zarifi, A. Mohammadpour, S. Farsinezhad, B. Wiltshire, M. Nosrati, A. Askar*, et al.*, "Time-resolved microwave photoconductivity (TRMC) using planar microwave resonators: Application to the study of long-lived charge pairs in photoexcited titania nanotube arrays," *The Journal of Physical Chemistry C,* vol. 119, pp. 14358-14365, 2015.
[122] E. Iravani, S. A. Allahyari, Z. Shojaei, and M. Torab-Mostaedi, "Surface Modification and Spectroscopic Characterization of TiO2 Nanoparticles with 2-Aminoethyl Dihydrogen Phosphate," *Journal of the Brazilian Chemical Society,* vol. 26, pp. 1608-1616, 2015.
[123] R. Luschtinetz, G. Seifert, E. Jaehne, and H. J. P. Adler, "Infrared spectra of alkylphosphonic acid bound to aluminium surfaces," in *Macromolecular symposia*, 2007, pp. 248-253.
[124] G. Zorn, I. Gotman, E. Gutmanas, R. Adadi, G. Salitra, and C. Sukenik, "Surface modification of Ti45Nb alloy with an alkylphosphonic acid self-assembled monolayer," *Chemistry of Materials,* vol. 17, pp. 4218-4226, 2005.
[125] M. Abkowitz, "Time-resolved dark injection from various metals into an amorphous semiconductor," *Journal of Applied Physics,* vol. 50, pp. 4009-4014, 1979.